Georgia State University

ScholarWorks @ Georgia State University

12-12-2022

Imaging non-Uniform Stellar Surfaces

Caleb G. Abbott
Georgia State University

Follow this and additional works at: https://scholarworks.gsu.edu/phy_astr_diss

Imaging non-Uniform Stellar Surfaces

by

Caleb G. Abbott

Under the Direction of Fabien R. Baron, PhD

A Dissertation Submitted in Partial Fulfillment of the Requirements of

Doctor of Philosophy

in the College of Arts and Sciences

Georgia State University

2022

ABSTRACT

There exists, in astronomy, many methods and techniques for observing stars. However, many of these observations treat the stars as point sources, infinitesimally small points of light. This is of course not how these objects are in reality, and is merely the limit of how they are seen from Earth. In reality, many if not all of these stars have some manner of spotted surface with ever changing features. We present here a study of these spotted stars, and how to recreate maps of their surfaces, in three unique but ultimately interconnected projects. First, we observe a sampling of Asymptotic Giant Branch (AGB) stars of various spectral types. We image these old, large, and spotted stars with the CHARA array; using the data gathered to determine their angular and physical sizes, thus helping narrow down or confirm masses and other parameters and lay the ground work for images of their surface reconstruction. With light-curve inversion (LI), we present our open source code for integrating the Alternating Direction Method of Multipliers with previous methods and a robust simulator for producing complex light-curves of spotted stars. Results are compared to other reconstructions of real data and match the other findings with great promise. Next, we discuss the Advanced Reconnaissance of Earth-orbiting Satellites (ARES) atmospheric turbulence simulator. Atmosphere effects generated with ARES match the expectations set for a wide range of turbulence, tested for D/r0 between 5 and 80, and sport the capability of simulating non-point source objects. This work endeavors to show the interconnected nature of all these topics as a study of imaging spotted stars.

INDEX WORDS: Astronomy software, High angular resolution, Instrumentation, Observational astronomy, Optical interferometry, Starspots

Imaging non-Uniform Stellar Surfaces

by

Caleb G. Abbott

Committee Chair:	Fabien R. Baron
Committee:	Stuart M. Jefferies
	Claudia Paladini
	Russel White

Electronic Version Approved:

Office of Graduate Studies

College of Arts and Sciences

Georgia State University

December 2022

DEDICATION

I dedicate this dissertation to my loving parents: Gregory and Rebecca Abbott. To my brother and his family: Cole, Holly, Lilly, and Kai Abbott. And to all those and more family, friends, and colleagues that helped support me throughout my collegiate career.

ACKNOWLEDGEMENTS

Each inspired and challenged me in their own unique way that I'll forever be grateful for. I'd also like to thank Dr. Claudia Paladini for her support and guidance during my trip to Chile and the stressful times trying to get back when the globe was beginning to lock down; and of course for her insight and expertise on AGB stars. Lastly, but not least, I'd like to thank Dr. Russel White for his teachings during class, his aid as the Astronomy Graduate Director, and his aid in this thesis. I would also like to thank Dr. Monica Valluri, whom I worked with at the University of Michigan as an undergraduate student. She helped build my confidence in research and set me on the path to meet the great people at GSU.

I'll end these thanks, though there are certainly more due, with a quote from my favorite story.

All we have to decide is what to do with the time that is given to us.

-J.R.R. Tolkien, The Fellowship of the Ring

TABLE OF CONTENTS

LIST OF TABLES

LIST OF ABBREVIATIONS

ADMM	alternating direction method of multipliers
AGB	asymptotic giant branch
AO	adaptive optics
ARES	Advanced Reconnaissance of Earth-orbiting Satellites
CHARA	Center for High Angular Resolution Astronomy
cm	centimeter
dec	declination
DM	deformable mirror
EPLL	Expected Patch Log Likelihood
ESO	European Southern Observatory
GPU	graphics processing unit
HB	horizontal branch
ISM	interstellar medium
JPL	Jet Propulsion Laboratory
KB	kinematic base
LCoS	liquid crystal on silicon
LEO	low-Earth orbit
LGP	light-gathering power
LGS	laser guide star
MIRC	Michigan InfraRed Combiner
MIRC-X	Michigan InfraRed Combiner, Exeter
MYSTIC	Michigan Young STar Imager at CHARA
μ**m**	micron
mas	milliarcsecond
mm	millimeter
MS	main sequence

NLopt	nonlinear optimization
nm	nanometers
ObGen	object generator
OITOOLS	Optical Interferometry Tools
PSF	point spread function
RA	right ascension
RGB	red giant branch
ROTIR	ROTational Image Reconstruction
RMS	root mean square
SDA	space domain awareness
SIMTOI	SImulation and Modeling Tool for Optical Inteferometry
SLM	spatial light modulator
SSIM	structural similarity index measure
TESS	Transiting Exoplanet Survey Satellite
TV	total variation
VLTI	Very Large Telescope Interferometer
WFS	wavefront sensor
ZODS	zero-order diffraction spot

Chapter 1
INTRODUCTION

In this chapter we will lay down the foundation for the topics discussed throughout this manuscript. Section 1.1 goes over the basics of interferometry and, our targets of interest, AGB stars. Section 1.2 covers Light-curve inversion. Section 1.3 details the Alternating Direction Method of Multipliers (ADMM) algorithm. In Section 1.4 we will discuss the background and parts important for instrumentation projects. Lastly, Section 1.5 reviews the statuses of the projects discussed throughout this work.

1.1 Interferometry and AGB Stars

Here follows an overview of interferometry and (the targets of interest in this manuscript) Asymptotic Giant Branch (AGB) stars. For a more thorough coverage of AGB stars we direct the reader to Habing & Olofsson (2004), with note to the chapter by Lattanzio & Wood (2004), and Paladini (2011) for further reading and from where this text on AGBs is based.

1.1.1 *An Introduction to Interferometry*

Interferometry, stated simply, is using many smaller telescopes, combined together in some array, to mimic and exceed the resolution of very large (and thus, very expensive) standard telescopes. A deeper dive into why this is can be found in sources such as McAlister et al. (2005) and ten Brummelaar et al. (2005). To see how the difference in resolutions manifests see Equations 1.1 and 1.2 where the theoretical resolution of a singular and multiple telescope setup are shown respectively.

$$\theta \approx 1.22 \frac{\lambda}{D} \tag{1.1}$$

1

Here θ is the angular resolution (in radians), D is the diameter of the telescope in meters, and λ is the wavelength being observed (once again, in meters). For an interferometric array, however, the angular resolution will go as:

$$\theta \approx \frac{\lambda}{2B} \tag{1.2}$$

Where B is the "baseline" or the distance between two telescopes (in meters).9

So while a $1m$ telescope, at 1630μm (H-band), would have a resolution of $\theta = 410$ arcseconds, two $1m$ telescopes separated by $300m$ would now have a resolution of $\theta = 0.56$ arcseconds. This is, again, the equivalent of having a telescope with almost $D = 750m$; which, obviously, a singular telescope of such a size is difficult if not impossible from a financial standpoint let alone a structural one. There are efforts to make these larger and larger telescopes with segmented mirrors (Nelson et al. 2013) but there is still a ways to go before they match what some modern interferometers are capable of.

Of course, this resolution does not come freely. In addition to the increased complexity of properly recombining the light from the two telescopes, there still remains the difference in light gathering power (LGP). Since the LGP is still dependent on the size of the individual telescopes interferometry is biased towards brighter objects, as these will be easier to see given the (relative to the resolution) smaller LGP. It is for this reason, as will be discussed later in Section 1.1.2 and 2.1 that our targets are chosen thusly for their angular extent and brightness.

Interferometry has continued to be on the rise with more and more sites being setup across the globe. And while each one has its specialities, all worthy of note, the focus of this work will be on the interferometers used for making the observations: the Center for High Angular Resolution Astronomy (CHARA) array and the Very Large Telescope Interferometer (VLTI).

1.1.2 *Asymptotic Giant Branch Stars*

AGB stars are one of the steps on the evolutionary track for stars between $1-8M_\odot$. After the star leaves the Main Sequence (MS) it proceeds down the giant path: through the Red Giant Branch (RGB), the helium flash leads onto the Horizontal Branch, while continued helium burning leads to the star rising up the AGB. Specifics of this whole process of course lie in the mass and composition of star(s) in question. As AGB stars are one of the main focuses of this work we will focus on fleshing out those details herein. And while there are many intracies and interesting avenues one could examine with AGB stars, the characteristics examined most in this work are the various types of AGBs (with emphasis on the Carbon AGBs, see Section 2.1), angular size (Section 2.3, and the stellar outflows that lead to enriching the ISM.

Working from the inside-out, the structural breakdown of an AGB star is: a dense carbon and oxygen core, shells alternatively burning Helium and Hydrogen, a large stellar envelope, and finally a layer of atmosphere before a very large, and cool, circumstellar envelope. Thermal pulses will occur as the He and H shells swap burning phases; at the same time a phenomena known as the third dredge-up may occur. During this the atmosphere is enriched with the results of He-burning, namely carbon. And, depending on the effectiveness of the dredge-up, the Carbon abundance may overtake the Oxygen abundance; this is what we call a carbon-star (C-star). Two other "flavors" of AGBs are: when $C/O < 1$ this is an M-type star (De Beck & Olofsson 2018), and $0.5 < C/O < 1$ is an S-type star (Jorissen et al. 1993; van Eck et al. 2011).

All these pulsations, it is thought, lead to shock-waves being sent through the atmosphere. The gas is lifted upward and then radiation pressure accelerates it away (Fleischer et al. 1992; Hoefner & Dorfi 1997; Willson 2000). The stellar wind will not be spherical in distribution, but take more complicated geometries (Freytag & Höfner 2008). Additionally, the mass-loss rate may not be static: the initial mass-loss could lead to heating of the dust formation zone due to less efficient cooling, reducing the formation of dust and leading to a reduced mass-loss

rate. This may produce episodic mass-loss, an effect clearly seen in radiation-hydrodynamic models of carbon-rich stars (Eriksson et al. 2014). It is important to observationally establish the detailed stratification and geometry of the extended atmosphere and to compare it to different modeling attempts.

1.1.3 *The Importance of AGB Stars and Interferometry*

As mentioned in Section 1.2.1 and in the above Sections the importance of AGB stars (from the perspective of this manuscript) is the enrichment of the ISM that leads to the heavier elements that are necessary building blocks for our world and ourselves. Optical interferometry is needed to study these effects as it is one of the only methods with high enough resolution to resolve the surfaces of these stars.

Thanks to the spatial resolution of optical interferometry it is possible to resolve the inner atmosphere of AGB stars where asymmetric structures may form. Until few years ago model-fitting dominated most of AGB studies (Paladini et al. 2009), but the very first images of AGB stars are now starting to emerge in the literature (Monnier et al. 2014; Wittkowski et al. 2017; Paladini et al. 2018a). C-type AGBs, such as R Sculptoris, tend to be more obscured by dust than S- or M-type stars such as π^1 Gruis. Stronger asymmetries have historically been detected in the near-IR for carbon-rich stars (Wittkowski et al. 2011; Cruzalèbes et al. 2013; van Belle et al. 2013) due to dust partially obscuring the stellar surface. O-rich dust is transparent in the near-IR, enabling studies of the molecular environment and convection patterns; to this end CHARA will be instrumental.

Further more, with instruments such as GRAVITY (on the VLTI, GRAVITY Collaboration et al. 2017), which has a massive amount of spectral channels (over 1700), it is becoming possible to delve further and learn more about these evolved stars.

1.2 Light-Curve Inversion

One method for obtaining a reconstruction of stellar surfaces is brought about by the examination of the star's light-curve making use of Light-Curve Inversion (LI) techniques (Harmon & Crews 2000; Cowan et al. 2013). LI works by looking at the changes over time in the intensity readings from a star and mathematically inferring the location of the relatively dim spots. There is a lot of difficulty in LI as it is inherently difficult to distinguish spots and features from the noise as well as being dependent on the input values for inclination, rotational velocity, and the like. Such processes have been examined and tested since LI's inception (Harmon & Crews 2000; Roettenbacher et al. 2011, 2013) so we shall in this manuscript briefly recap the relevant items. At its core, LI works by creating brightness patches across a surface map that (with a given observation angle, geometry, etc.) best re-produces the observed flux from the light-curve. LI has farther reaching uses than just stellar surface reconstruction as shown by Majeau et al. (2012) with mapping the surface of an exo-planet.

The benefits of following this method are twofold: the number of spots do not need to be known beforehand and the light-curve itself does not need to be uniformly sampled. These two things allow us to circumvent a couple of the restrictions/difficulties that have existed in LI throughout its iterations. Meanwhile, some unknown parameters that lead to ambiguities/issues in the reconstruction are: limb darkening, inclination angle, and the shape of the star. The rotation period is also an important parameter with one way of determining it by observing the periodic oscillations of the light-curve; this being one of the reason why, with LI, one is limited to objects rotating fast enough that the surface features do not change drastically between rotations.

The first of these unknown parameters we'll tackle is the effect of limb darkening and some ways in which we might deal with the issue. The problem with limb darkening is its obvious effect on the brightness of spots/features towards the edges of the star. To avoid this, LI inversion methods produce temperature maps instead of intensity ones, as these should

be unaffected by limb darkening which have the apparent effect of reducing the intensity seen by the observer. There are, however, some benefits in that their location on the stellar surface can be narrowed down some. Spots towards the edge of the star have their intensity affected more by the limb darkening, appear dimmer, and thus have their effect on the light curve reduced. Meanwhile, spots away from the edges will show a relatively greater intensity drop to the surrounding stellar surface. Within our codes (Baron & Martinez 2018) there are several different limb darkening laws that can be implemented (quadratic, linear, square-root, power, and etc.).

The impact of the star's inclination angle is another one of the main ambiguities when performing LI. Without data beyond the light curve itself one does not know the true surface of the star and so must use a range of inclinations in the reconstruction. Multiple wavelengths with the photometry can alleviate the problem, however one of the main sources of light curves, *Kepler* (Borucki et al. 2010), lacks multiple wavebands. As well, there are ways to estimate the inclination of a star, such as with Asteroseismology (Gizon & Solanki 2003; Gehan et al. 2021); such methods though experience issues when stars are close to pole-on or equator-on, Reconstruction quality of a light-curve is dominated by inclination ambiguity and not by signal-to-noise ratio issues.

As previously mentioned, we are somewhat limited in what objects we can reconstruct with LI. The star, in our case, needs to rotate fast enough compared to the lifetime of the spot so that changes to the stellar surface over the course of one rotation are minimized; as well one generally needs several rotations to recover a surface. With these in mind we choose our test target from those observed by the *Kepler* mission as well as adjust the parameters of our simulations to match.

Beyond the current state of LI there have been some recent progress in Luger et al. (2019) with STARRY in using harmonics. One of the main limitations of current methods, however, is the resulting reconstructions are all snapshots of the stellar surface. In this work, and moving forward, we want to evolve this towards a full movie of the stellar surface to be

able to see the evolution of the spots. To do this, we need to make use of matrix sparsity (diagonal matrices, etc.) for a more efficient way of computing the reconstruction along with implementing various regularizers. Regularizers are terms that reduce the complexity of a solution by imposing a penalty on certain parameters. The three main regularizers utilized in this work are: temperature regularizer, smoothness in the spatial plane, and temporal smoothness.

The first regularizer, the temperature scaling one (or what we refer to as the Harmon regularizer) penalizes extreme departures from the temperature of the photosphere and can be tuned to prefer bright or dim spots in the reconstruction (Harmon & Crews 2000). Spatial smoothness is penalized via Total Variation (TV), or the 2-D spatial gradient of the stellar surface. This exists as the stellar surface should be mostly smooth, and so the derivative of the reconstruction is penalized to be lower. Lastly, the temporal regularizer exists so that reconstructions are penalized to be similar to other reconstructions close to them in time; we include this in effort to again return a full movie and better tie each frame to those around it. These last two regularizers, the spatial and temporal smoothing, are new additions to the classic LI formula. In order to implement these new regularizers and enforce sparsity we've decided to make use of the Alternating Direction Method of Multipliers (ADMM), detailed in Section 1.3, as our tool to reduce the reconstructed images efficiently.

Another method for reconstructing LI has been endeavored by Luger et al. (2019) with STARRY by using harmonics. Into the future we hope to see other numerical methods used with and compared with ADMM such as Gaussian Mixture Models (Deledalle et al. 2018), Patch Prior (Zoran & Weiss 2011), and Student T-Mixture (Van Den Oord & Schrauwen 2014).

1.2.1 *The Importance of LI*

LI is important as it gives astronomers one further avenue to draw out information on the star being examined. Furthermore, as will be touched upon again in Section 1.1.2, the spots and

other features revealed by LI play can be key pieces into the enrichment of the InterStellar Medium (ISM); and thus the pieces that make up you and me.

1.3 Alternating Direction Method of Multipliers

ADMM is a useful numerical method for splitting up and solving a large, complicated, inverse problem (such as a reconstruction) and turning it into multiple, but simpler, iterative equations with known solutions or other means of solving (Simões et al. 2016; Figueiredo & Bioucas-Dias 2010; Xu et al. 2017). These known solutions are known as Proximal Operators (Schutz et al. 2014) and are detailed further in this paper. Further advantages of ADMM are parallelization, positivity, and noise (such as Poisson) can be taken into account even at low fluxes. ADMM is a useful tool in optimization problems such as image denoising, as well as deblurring (Chan et al. 2011), and will be shown to be useful in LI. One of the strengths of ADMM is how it splits the optimization into smaller problems that are done in tandem.

The main equation we're attempting to solve for our image restoration problems is shown in Equation 1.3 with Total Variation (TV) included as our first regularizer.

$$I = \underset{x \in \mathbb{R}^{N \times N}}{\arg\min} \quad \frac{\mu}{2} \|Ax - y\|^2 + \|\nabla x\|_1 \tag{1.3}$$

Here y represents the observed data, x the original data (and the target of our reconstructions), A is some transformation matrix, μ is the noise, ∇x is the 2D spatial derivative of x, and I is the reconstructed image. The $\|\|$ here represent the operator norm. The first step of ADMM is to substitute a new variable, z, for ∇x (Eqn. 1.4).

$$I = \underset{x}{\arg\min} \quad \frac{\mu}{2} \|Ax - y\|^2 + \|z\|_1 \quad \text{with} \quad z = \nabla x \tag{1.4}$$

Where z can be a multi-dimensional matrix with components in the (x,y,t) directions (as seen in Eqn. 1.5; here the uplifted T represents a transposed matrix).

$$z = [z_x^T \quad z_y^T \quad z_t^T]^T \qquad (1.5)$$

This allows the equation to then be solved using the extended Lagrangian method (Liou 1995) and is shown in Equation 1.6; adding in the minimization of z to ∇x in addition to the Lagrangian variables (Chan et al. 2011; Schutz et al. 2014). We also add an adjustable weight to the TV term (λ_{TV}) for further control over the smoothness of the image.

$$L(x, z, u) = \frac{\mu}{2} \|Ax - y\|^2 + \lambda_{TV} \|z\|_1$$
$$-u^T(z - \nabla x) + \frac{\rho_r}{2} \|z - \nabla x\|^2 \qquad (1.6)$$

With Equation 1.6 we then begin solving $L(x, z, u)$ by iteratively minimizing/updating each of its three arguments: x, z, and u (where u is the scaled Lagrangian multiplier introduced as part of the extended Lagrangian method). The three iterative solution steps are shown here with the subscript k denoting the iteration number:

1.

$$x_{k+1} = \arg\min_x \frac{\mu}{2} \|Ax_k - y\|^2$$
$$-u_k^T(z_k - \nabla x) + \frac{\rho_r}{2} \|z_k - \nabla x_k\|^2 \qquad (1.7)$$

2.

$$z_{k+1} = \arg\min_z \lambda_{TV} \|z_k\|_1$$
$$-u_k^T(z_k - \nabla x_{k+1}) + \frac{\rho_r}{2} \|z_k - \nabla x_{k+1}\|^2 \qquad (1.8)$$

3.

$$u_{k+1} = u_k + \rho_r(\nabla x_{k+1} - z_{k+1}) \qquad (1.9)$$

The first steps involve minimizing with respect to x, and then z, by calculating $\nabla_x L$ and $\nabla_z L$. By solving these for x and z respectfully, two iterative solutions are found (Eqns. 1.10 and 1.11).

$$x_{k+1} = \frac{\mu A^T y + \rho_r \nabla^T z_k - \nabla^T u_k}{\mu A^T A + \rho_r \nabla^T \nabla} \tag{1.10}$$

Next, solving for z_{k+1} (Eqn. 1.8) we can use a known proximal operator using the shrinkage formula (Liu et al. 2013):

$$z_{k+1} = \max(0, (|z_0| - \frac{\lambda_{TV}}{\rho_r}) * \text{sign}(z_0) \tag{1.11}$$

Where $z_0 = \nabla x_{k+1} + \frac{u_k}{\rho_r}$.

The last step is to update the scaled Lagrangian multiplier, u, by feeding it the updated x_{k+1} and z_{k+1} (Equation 1.9).

We then allow this loop to run until either maximum iterations are met (mostly used for testing purposes), the difference between iterations x_{k+1} and x_k are below some preset threshold, or a χ^2 threshold to break the loop.

1.3.1 *Other Regularizers*

The above solutions and equations include only the TV regularization, but there are many more regularizers one can choose to include (with the draw back of added complexity of course). Here we detail two other options included in the final code: mask and temporal regularization. A mask's normal function is to specify a pixel area for reconstruction assuming prior knowledge of shape of the object and focuses the code to only reconstruct within that space (i.e. knowing a star is circular and how large it would be on the pixel grid) and is represented by a binary vector of 1's and 0's (where a pixel matching with a 1 is included within the reconstruction and a 0 is not).

$$z_{m,k+1} = \begin{cases} Z_m * x_{k+1} & if\, Z_m \cdot M > 0 \\ 0 & else \end{cases} \tag{1.12}$$

$$u_{m,k+1} = u_{m,k} + \rho_m(\nabla x_{k+1} - z_{m,k+1}) \tag{1.13}$$

Here, M is our binary mask function and $Z_m = x_{k+1} + \frac{u_m}{\rho_m}$. This, by itself, is not very useful for our purposes here with LI, as the entirety of the array is the surface of our star, but it does provide other benefits. A side effect of the mask though is its enforcement of positivity (Schutz et al. 2014) as seen in Eqn 1.12 where the code (while within the area specified by the mask, M) enforces the reconstruction to be 0 or above. When the shape or extent of the reconstruction region isn't known you can simply substitute the mask array for a field of ones and the entire image area will again be considered for reconstruction though with positivity still enforced. This is what we use here, when including the mask regularization, as we are reconstructing all of the stellar surface and thus all parts of the image array (x) are filled. However, this could be used to further restrict the reconstruction to only focus on pixels of the temperature map that are visible to the observer at that time as well.

As mentioned before, the more regularizers you add the more complex the routine becomes and thus will change our equation(s) for LI even further. The updated Lagrangian Equation is shown in Equation 1.14.

$$
\begin{aligned}
L(x, z, u, z_m, u_m) = {} & \frac{\mu}{2} \|Ax - y\|^2 + \lambda_{TV} \|z\|_1 - u^T(z - \nabla x) \\
& + \frac{\rho_r}{2} \|z - \nabla x\|^2 - u_m^T(z_m - x) + \frac{\rho_m}{2} \|z_m - x\|^2
\end{aligned}
\tag{1.14}
$$

Where ρ_m is the regularization weight for the mask and u_m is its Lagrangian multiplier.

Yet another regularizer, and the one necessary for allowing this to be a dynamic approach to LI, is the temporal aspect. That is to say linking each epoch or image not only to itself (as in the spatial, TV, regime) but also linking consecutive epochs in the time domain to enforce a more cohesive and smooth reconstructed "movie" for the data. For this purpose here we invoke a method like that shown in Schutz et al. (2014) for spectral regularization that we adapt here to be used as a temporal regularization. These regularizations are effectively the same by thinking of our datacube in time as being analgous to one of wavelength; the

Equations 1.15 - 1.20 detail the updated Lagrangian equation and the iterative equations for the temporal regularizer.

$$L(x, z, u, z_m, u_m) = \frac{\mu}{2} \|Ax - y\|^2 + \lambda_{TV} \|z\|_1 - u^T(z - \nabla x)$$

$$+ \frac{\rho_r}{2} \|z - \nabla x\|^2 - u_m^T(z_m - x) + \frac{\rho_m}{2} \|z_m - x\|^2 \qquad (1.15)$$

$$+ \frac{\rho_t}{2} \|z_t - u_t\|$$

$$z_{t,k+1} = [\nabla^t \nabla^{t,T} + I_{N_t}]^{-1} [(V_t - \frac{u_{V_t}}{\rho_t})\nabla^{t,T}$$

$$\qquad (1.16)$$

$$+ (x_{k+1} + \frac{u_t}{\rho_t})]$$

$$V_{t,k+1} = \arg\min_{V_t} \lambda_t(V_t) + \frac{\rho_t}{2} \|V_t - V_{t,q}\|^2 \qquad (1.17)$$

$$V_{t,q} = z_{t,k+1}\nabla^t + \frac{u_{V_t}}{\rho_t} \qquad (1.18)$$

$$u_{t,k+1} = u_t + \rho_t(x_{k+1} - z_{t,k+1}) \qquad (1.19)$$

$$u_{V_t,k+1} = u_{V_t} + \rho_t(z_{t,k+1}\nabla^t - V_{t,k+1}) \qquad (1.20)$$

1.3.2 The Importance of ADMM

ADMM is important not just as a minimization algorithm but as step towards even more advanced techniques. ADMM allows for relatively simple execution of parallelization, this speeds up the processes by sending them to separate cores as each sub-problem is an independent problem. This parallelization, along with other aforementioned factors, also makes ADMM a great stepping stone towards more complex algorithms such as Expected Patch Log Likelihood (EPLL) and other machine learning techniques. Further evolving our code and methods to these more advanced ones is one of our future goals for this project.

1.4 Instrumentation and Atmospheric Simulation

Here is described an overview of the hardware pieces, concepts, and procedures important to our instrument systems. We start with an overview of the main components used in our instruments, a discussion of the phase screens we implement to mimic atmospheric turbulence, and end with going over how we use standard optics (i.e. lenses) to get the most out of our system.

Our main focus in builidng and using instruments in this work is for improving Space Domain Awareness (SDA), the study of objects (especially satellites) near and around the Earth. capabilities. However, all the methods and experience utilized herein have equal application to broader astronomical and scientific studies and is discussed further in Chapter 4.

1.4.1 *Spatial Light Modulators*

Spatial Light Modulators (SLMs) are an opto-electro device with many applications in optics and instrumentation. The SLMs used in our setups are of Meadowlark design; having a 1152 by 1920 pixels (each pixel being 9.2 μm) Liquid Crystal on Silicon (LCoS) reflecting surface. Amongst our SLMs are also versions with different refresh rates at, what we call, High-speed (555 Hz) or Mid-speed (83 Hz) SLMs. SLMs work by applying a voltage across the LCoS, which are arranged in a homogeneous configuration, with the voltage causing the affected nematic liquid crystals (LC) to rotate. This rotation, in essence, changes the index of refraction of that pixel which causes incident light to be phase shifted upon reflection off the backpane of the SLM surface (assuming the light is polarized to match the fast axis of the LCoS surface). The result of this is per pixel phase control across the entire surface of the SLM.

To program the phase distortions upon the SLMs a phase screen (PS) is loaded, via software, across the LCoS. More details on PS generation are covered in a later section

(Section 1.4.3). An important hardware limitation of the SLMs used in our setups is each LC being limited to 256 discrete voltage levels and limited to 0 to 2π phase shifts. The effect of this on the system is the limit to 8-bit bitmap (BMP) files for our PS and the necessity of phase wrapping; phase wrapping here is the system of keeping the phase within the set limits by "resetting" the phase modulation. That is to say as the phase exceeds 2π the value is reset back to 0, so a programmed shift of 3π is input as a shift of only π (5π to π as well, 3.5π to 0.5π, and so on).

A thorough breakdown of SLMs can be found in Lazarev et al. (2019) and within the manual(s) provided by Meadowlark (Meadowlark 2019).

1.4.2   *Deformable Mirrors and Adaptive Optics Systems*

Deformable Mirrors (DMs) consist of a thin reflective sheet atop an array of actuators that can push and pull the sheet to alter light incident upon its surface. When paired with a Wavefront Sensor (WFS) one can create an Adaptive Optics (AO) system loop. The components we use are from ALPAO with two main systems composed of DM-97-15s and DM-241s, having 97 (11 across the aperture) and 241 total actuators respectively (ALPAO 2021).

While DMs are mostly used for correcting a given wavefront, when paired into an AO system, they can also be used independently to impose wavefront distortions. This is in part something we shall discuss further in Section 4.1.1. For our systems we use high-speed Shack-Hartmann sensors, included from ALPAO, to detect the wavefront aberrations and, with the software, issue the commands to the DM to correct it.

1.4.3   *Phase Screens and Turbulence*

We generate static phase screens using a standard Fourier transform power spectrum filter function approach. First we create a 2D complex array of random numbers where the real and imaginary components of the array are generated from a Gaussian distribution with

mean $= 0$ and standard deviation $\sigma = 1$. Second, we multiply this array by the amplitude of the wavefront phase spectral density given by:

$$A_\phi(i, j) = 0.151 \ (2D/r_0)^{5/6} \ (i^2 + j^2)^{-11/12}. \tag{1.21}$$

where i and j are the sample indices, D is the diameter of the telescope aperture, and r_0 is the Fried parameter (Lane et al. 1992).

Third, we set the D.C. (i.e. zero spatial frequency) bin to zero to ensure a zero mean phase at the end of the process. Fourth, we inverse Fourier Transform the resultant array to produce two independent realizations of a Kolmogorov phase screen: one in the real part of the transform, the other in the imaginary part.

We note that, for the simulated screen to be accurate over the aperture we are interested in, we need to generate the screen on an array that is at least four-times larger than the aperture. This is necessary for two reasons.

First, we need to use a number of points in the simulation that can capture the outer scale length of the turbulence L_0 that typically has a value of around 15 to 25 m, depending upon the site (Sedmak 2004). Without this, the low spatial frequencies are not adequately represented and the observed phase structure function for the phase screen does not well represent the expected phase structure function

$$D_\phi(\rho) = 6.88 \left(\frac{|\rho|}{r_0} \right)^{5/3} . \tag{1.22}$$

Here $|\rho|$ is the spatial length scale between points in the phase screen. Second, using the Fast Fourier Transform (FFT) approach for generating a phase screen results in phase screens that are periodic in x and y and which do not appear to have any apparent overall slope. This is not realistic. However, the shortcoming can be mitigated by only using the central section of the screen.

A wavefront evolves both spatially and temporally. This results in spatial and temporal correlations in a set of wavefronts that are measured over an interval that is commensurate with, or less than, the atmospheric coherence time:

$$\tau_0 = 0.314 \ r_0/\bar{V} \ , \tag{1.23}$$

where $\bar{V}$ represents a weighted average of the wind velocity over the height range of the turbulence.

We use the approach of Dayton et al. (2018) to capture the spatial and temporal correlation behavior in the wavefront. In their approach the primary spatial evolution is near frozen flow translation due to wind speed. After translating the phase screen to account for the frozen flow behavior, the shifted phase screen is updated with a new phase screen generated with an independent array of complex numbers, using the auto-regressive average algorithm:

$$\Phi_{update} = \alpha\Phi_{shift} + (1 - \alpha)\Phi_{new} \tag{1.24}$$

where α is the auto-regressive parameter. This parameter dictates the level of temporal and spatial evolution in the wavefront.

Using these phase screens, we can begin to simulate atmospheric turbulence with our SLMs. Turbulence here is measured by the ratio D/r_0, where D is the diameter of the telescope aperture and r_0 is the atmospheric coherence length for the observations. We model the turbulence screens in the ARES simulator with a resolution of $\sim$4 pixels/r_0 value. This means that for a beam size of $\sim$800 pixels in diameter on the SLM, we can, in principle, generate turbulence of up to $D/r_0 \sim$200; corresponding to very strong turbulence for almost any given telescope.

1.4.4 *Optical Relays and Alignment Techniques*

One of the main foundations upon which our instruments, detailed in Chapter 4, is the usage of what's known as a 4F system (a basic schematic of a 4F is shown in Figure 1.1). A 4F system, also known as an optical correlator, have many uses built around the effects of Fourier Optics. What we use 4F systems for in our system is for relaying the pupil plane so that, from the perspective of the system, the various components (DM, WFS, SLM, and etc.) are conjugated to each other. That is to say that there will be no effects of propagation between the optics, thus preserving details of the phase screens (and the quality of the alignment) that we put into the system. This will prove extremely important when in Chapter 4 (Section 4.1.1, specifically) we move away from the 4F system to introduce propagation effects between the components. Equation 1.25 details how one determines where the optics need be placed to properly relay the object plane to the new image location.

$$d_I = f_2 * (1 + \frac{f_2}{f_1} - d_O * \frac{f_2}{f_1^2})$$ (1.25)

Here, d_I is the distance from the last optic where the image is relayed to, f_2 is the focal length of the second lens, f_1 is the focal length of the first lens (first and second being relative to the direction in which the light is travelling, in this case), and d_O is the distance from the object plane (or the plane you are trying to relay to a new position). So, for an example: with $d_0 = 180mm$, and two lenses with $f = 100mm$, the image distance would be $d_I = 20mm$ from the second lens. Of course a 4F need not be made with two lenses of the same focal length. One can impose a magnification dependent upon the ratio of the focal lengths of the lenses (Equation 1.26).

$$M = \frac{f_2}{f_1}$$ (1.26)

So that having $f_1 = 150mm$ and $f_2 = 50mm$ would relay the object plane ($d_I = 46.7mm$) and reduce the beam size by a third.
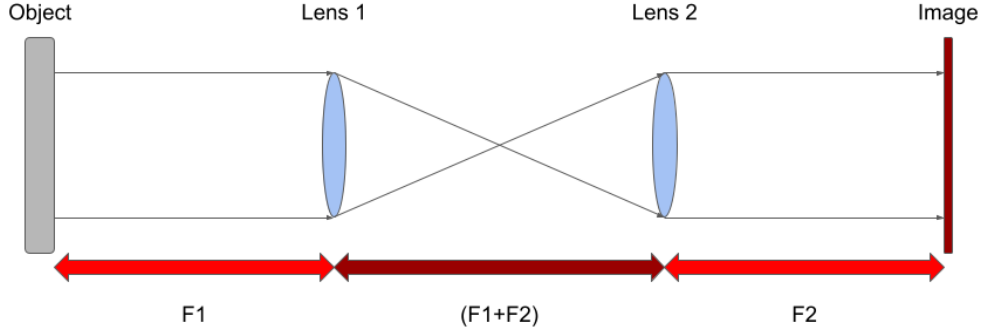
Figure 1.1 Diagram of a 4F optical system. It is important to note that the distance between the object and image is malleable; though the distance between the lenses must be consistent for collimation. As a part of this, while in most cases the total length of the 4F system will add up to the four times the focal length (or $2F_1 + 2F_2$ for different focal length lenses), this will not always be the case for lenses of different focal lengths (see Equation 1.25)

Individual lenses can be used to relay the pupil plane as well, although of course causing the beam to lose collimation. Equation 1.27 shows the distances required for a given focal length.

$$d_I = \frac{1}{\frac{1}{f} - \frac{1}{d_O}} \tag{1.27}$$

The variables used here are the same as those detailed earlier for Equation 1.25 with the obvious exception of having only one lens. For our purposes these single lens relay systems are mainly used for re-imaging the surface of the SLMs and/or DMs onto a camera for recording and alignment purposes.

On the topic of alignment, the 4F systems and other relay optics prove useful. While aligning normal optics, such as lenses, can be difficult to do with precision there may be a greater challenge in determining the location of our beam upon components such as the

18

SLMs. In our work the beam size is smaller than the reflective surface of the SLM, meaning that guaranteeing the beam is sampling the intended part of the SLM (where the phase perturbations are being applied) is of the upmost importance to ensure getting the desired results. Therefore, to help align the SLM we input a phase screen of an astigmatism cross (using Zernike polynomials) and, using it like a crosshair, use this to determine the center of our beam upon the SLM. This means that to align our system precisely, which necessitates having a clearly defined location of the beam, we need the crosshair used to be in as sharp of focus as possible; hence the use of relay optics to minimize/negate the effects of propagation that would otherwise begin to alter the look of the imposed phase screen. Of course other shapes and features can be used to determine the center and a solitary disk can be useful in determining both the center and size (in pixel space) of the beam.

1.4.5   *The Importance of Instrumentation*

The importance of instrumentation in general need not be stated, as without it our science and our society would not be as it is now. However, this specific application of instrumentation is important for (in the same vein of LI) getting the most out of the data scientists collect. From being able to do more observations from the ground, to improving our grasp on SDA, the instruments detailed herein prove a strong stepping stone to testing the next generation of instruments and the effects of the atmosphere itself on our lives; scientific, civilian, or otherwise.

1.5   Summary of Projects

In this manuscript we describe a wide array of projects; all with a focus on imaging (or alternatives to imaging in the case of LI) with an emphasis on spotted stars. The main goal of this work is to detail non-traditional methods of retrieving and reconstructing information from stars and other space based objects and bodies.

Chapter 2 describes the status of the data and analysis of AGB stars observed with the CHARA interferometric array. Here we will discuss the chosen targets and the results of determining the angular size of said targets. In Chapter 3 we discuss the combination of LI with the ADMM algorithm. Here we will cover the implementation of the algorithm, test it on a wide arrange of simulated data, and then invert the light-curves of real Kepler and TESS data. Chapter 4 details the instrumentation test-bed, ARES, which will provide a highly adaptable basis for simulations as well as testing new and future instruments. This chapter will also discuss some of said instruments and their various stages of completion. Lastly, Chapter 5 will conclude with a summary of the work shown herein as well as what future directions the research may be taken towards.

Chapter 2
INTERFEROMETRIC IMAGING OF AGB STARS

In this chapter we will discuss the observation and analysis performed for our study of AGB stars. Interferometry, specifically with the CHARA array, was chosen for its high resolution imaging being able to potentially see details of the stellar surfaces. The chapter is broken down such that: Section 2.1 covers the target selection, Section 2.2 details the observations performed, Section 2.3 shows the results from determining the angular sizes of the stars sampled, and lastly Section 2.4 covers our collaboration with the European Southern Observatory (ESO). Discussion of the results from this chapter are covered in Section 2.5.

2.1 Choosing a Target List

Targets were chosen so as to have a wider selection of types of AGBs; the intent being to compare the size and potential output of convective cells across the various "flavors" of AGB. Table 2.1 shows the list of targets, including a collaboration target with RZ Ari. The chosen targets were also picked in order to have a selection of stars viewable through the spring and fall observing semesters at CHARA (with a little overlap). The science driver for these targets were stars bright enough and large enough that we could build a sample of AGBs

All targets were observed with the Michigan InfraRed Combiner - eXeter (MIRC-X) instrument at the CHARA telescope array (see Section 2.2) along with later, yet un-examined, data being obtained concurrently with MIRC-X and Michigan Young STar Imager at CHARA (MYSTIC; Monnier et al. (2018)).

2.2 Observations

All observations discussed in this chapter, barring Section 2.4, are gathered with the MIRC-X instrument on the CHARA array. MIRC-X (Kraus et al. 2018; Anugu et al. 2018) is an upgraded version of the original MIRC instrument; able to gather data with better signal-to-noise due to upgrades to the camera and optics systems that makes use of all six telescopes

Table 2.1.   AGB Targets

Star	Spectral Type	Angular Size (mas)	Parallax (mas)	Radius ($R_\odot$)
Z Psc	C-N5 B	x	1.5643 ± 0.0539	x
SV Psc	S3-54-8 B	x	2.5421 ± 0.1066	x
S Cas	M5 D	x	1.0515 ± 0.0907	x
RV Mon	C4,5 C	x	1.6275 ± 0.0351	x
CR Gem	C-N5 B	x	0.9417 ± 0.03	x
HR Peg	S4+/1+	4.22 ± 0.09	2.1405 ± 0.0813	212.17 ± 9.24
ϕ Aqr	M1.5III	5.20 ± 0.08	14.3482 ± 0.2594	38.8 ± 0.92
V460 Cyg	C-N5	7.27 ± 0.27	1.6823 ± 0.1203	465.96 ± 37.55
UX Dra	C-N5	7.18 ± 0.08	2.1294 ± 0.0944	361.92 ± 16.54
DR Ser	C5,4	4.09 ± 0.07	0.907 ± 0.0321	484.11 ± 19.03
HK Lyr	C-N5	4.63 ± 0.14	1.1328 ± 0.0196	441.00 ± 15.36
RZ Ari	M6 III	10.27 ± 0.01	10.227 ± 0.584	107.91 ± 6.16

Note. — Here is the target list for our observations of AGB stars. Multiple stars of different Spectral Types were chosen to be able to compare the resulting surface features and details between different "flavors" of AGBs. All targets were obtained using the MIRC-X instrument on the CHARA array. The angular sizes of the stars was completed using OITOOLS, the results of which are visible in Figure 2.2. Parallaxes are obtained via GAIA DR3 (Gaia Collaboration et al. 2016; van Leeuwen et al. 2022), with errors being propagated when determining the physical size of the stars.

from the array. Of the many prism/grism options these observations were done with the grism190 mode (R = 190); this grism containing approximately 36 spectral channels.

Observations were gathered over a yearly and weekly cadence (as conditions and time allowed). Most stars were observed two nights in a row multiple times throughout the course of a month, to try and track any short term changes, with followup observations the following year. Though most of the stars fell into either summer (V460 Cyg, UX Dra, DR Ser, and HK Lyr) or winter (Z Psc, SV Psc, S Cas, RV Mon, and CR Gem) targets, stars such as ϕ Aqr and HR Peg were observable in either semester and so had a more frequent cadence of viewing than the rest of the sample. Summer targets had greater luck with weather and other observing factors and thus are the only ones with calculated angular sizes (Table 2.1 and Figure 2.2) from our program.

Some stars proved a unique, but fun, challenge in obtaining fringes for all six telescopes at CHARA. More details on this can be found in Section 2.3.1 along with Figure 2.1. The crux of the matter being that observing large targets, which most of the AGBs examined here are, causes less light to be observed by the longer baselines of CHARA and other interferometers.

2.3 Angular Sizes

The data obtained above was reduced and calibrated using the official MIRC-X Python reduction pipeline (Le Bouquin 2020). Details of the reduction process can be found within Anugu et al. (2020) and Martinez et al. (2021). Once the data finished the calibration step, and were checked for systematic errors, we began examining it using our group's analysis package, OITOOLS (Baron et al. 2019).

Figure 2.2, and Table 2.1, shows the results of determining the angular size (and limb darkening coefficients) by fitting a model to our data for each of the listed stars assuming a circular and limb darkened disk. Not all of the stars in our target list have had their size calculated, due to either bad/missing data (having worse luck with stars during the winter
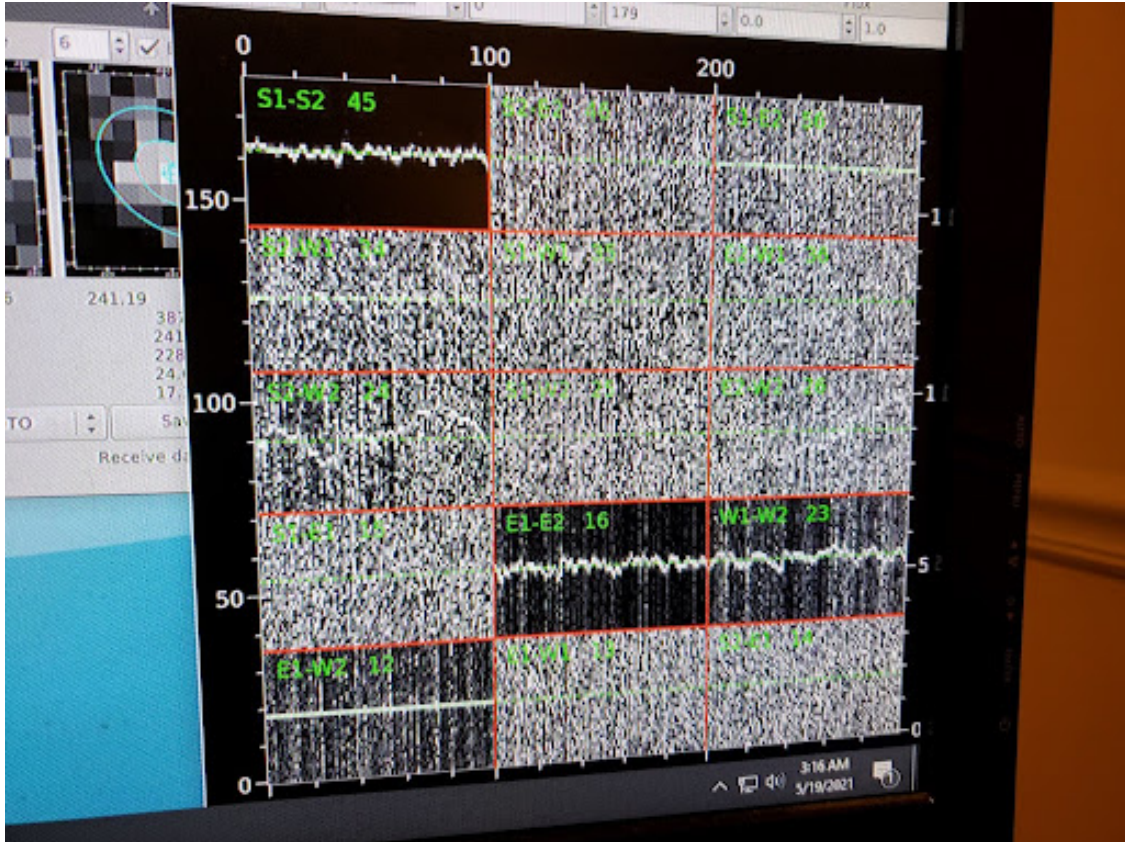
Figure 2.1 Here is an example showing the difficulty in observing a large star such as RZ Ari. The horizontal white line within each of the 15 (the total combinations of the six telescopes) regions is the fringe, from the interference of the two telescopes, and is invisible or very difficult to see above the noise in most of the combinations of scopes.

months) or waiting for future analysis. Further follow-up observations and analysis time will be required to round out our sample.

Table 2.1 also shows the value of the parallax (mas) and calculated physical radius (in solar units) for the stars. Parallaxes, found in GAIA DR3 (Gaia Collaboration et al. 2016; van Leeuwen et al. 2022) along with the provided errors, were used to determine the distance to each target. The physical radius of each star (for which we had determined an angular diameter) was then calculated simply by rearranging the formula for angular size to solve for the diameter/radius of the object instead. Errors for the parallax were then propagated along with the errors from the angular size determination (calculated from the spread of the distribution results from model fitting) to determine the errors for the stars' radii.

24

A standout star, both in terms of angular size and collaborative effort, is RZ Ari; detailed in the following Section 2.3.1.

2.3.1 *RZ Ari*

RZ Ari was a star added to our catalog in part do to a collaborative effort with the Bulgarian Academy of Sciences. RZ Ari is a fast rotating, apparently single, M giant of 2.2 $M_\odot$ that has evolved to the late RGB or early AGB stage. The science interest of the collaboration was, in part, in examining the long-term variability of the magnetic field, which was found and initially shown in Konstantinova-Antova et al. (2021). Our efforts in the collaboration were to confirm the angular and therefore physical sizes of the star with a further goal of reconstructing images of the stellar surface. The size of the star has been determined (final row, Table 2.1) while the imaging yet remains. Getting a surface image of RZ Ari will go far in helping prove certain theories about its variability; it being theorized that the variability of the star is in part due to a large-scale vortex in RZ Ari's atmosphere Käpylä et al. (2011).

RZ Ari proved a difficult, but admittedly fun, challenge to observe with MIRC-X in no small part due to its size. Figure 2.1 shows an example of how the fringes looked for RZ Ari when we were barely able to get all six telescopes. Why the size, which turned out to be around 10.26 mas (Figure 2.3), is the main culprit for this star's difficulty in being observed is for the same reason why large stars like Betelgeuse are difficult to see (at least the macro details) with the CHARA array and other interferometers. Though CHARA behaves effectively as a 330 meter telescope, it lacks telescopes close enough together to get closer to the center of the (U,V) plane (Figure A.13 for an example of the (U,V) coverage of one of our targets at CHARA). To see this in another way, Figure 2.4 shows the squared visibilities for the model (red) and data (black) of RZ Ari. In these sorts of plots, the different arches or "lobes" that the plot shows represent different characteristics of the star; of note, the first lobe gives us information on angular size of the star. And as can be seen in Figure 2.4, the first lobe (at the far left of the topmost plot) is almost not visible; and then with each

successive lobe the value of the squared visibility drops. What this means for us, in reference again to Figure 2.4, is that there is a lot less light within all but the shortest baselines of the array; and the data from those short baselines, that make up the first lobe, are clustered together and don't sample much of the lobe itself.

However, even with the challenge of getting the observations, the data we gathered for RZ Ari has proved useful in confirming the angular size (10.26 mas) of the star with high precision. This, along with distance estimates from GAIA DR3 of $D = 97.78pc$ (Gaia Collaboration et al. 2016; van Leeuwen et al. 2022), allows us deduce a radius of $R = 107.91R_{\odot}$ (Konstantinova-Antova et al. 2021). This is consistent with the luminosity, determined by Villaume et al. (2017), of $L = 1412L_{\odot}$. Errors for these values are shown in Table 2.1.

2.4 π Gruis

Another collaborative effort we have is with the European Southern Observatory (ESO) performing followup work, with new data, of Paladini et al. (2018a,b); the science interest of this target therefore being in part to compare images of the star and track any long term surface features. For this project, we took on the task of attempting to reconstruct an image of π Gruis given new data from the GRAVITY instrument. Gravity is an interferometric π Gruis is an S-type AGB star with a radius $R \approx 319R_{\odot}$ (Paladini et al. 2018a). We have three sets of data for the star: P60, P99, and P101; an example UV plot from the data is shown in Figure 2.5.

One of the biggest challenges here was in adopting the code and coming up with a way to visualize the over 1700 spectral channels boasted by GRAVITY. The images made previously for π Gruis were done using SQUEEZE (Baron et al. 2010) but we had wanted to run the reconstruction using the newer OITOOLS (Baron et al. 2019). Work still remains, detailed in Section 5.2.1, but we are excited at the prospect of new data and imaging techniques and the comparisons that can be drawn.

2.5 Discussion of AGB Results

Of the projects covered in this manuscript, this remains the one with the most future science to be explored. As it stands we have the angular sizes of over half our sample (Table 2.1 and Figure 2.2) and with GAIA distances we have calculated the physical sizes of these same stars with high precision; and with further reduction/calibration time the remaining targets are not far behind. The impact of not having the other half of the sample, at this time, is less confidence (when images are produced) that the surfaces we generate are typical of that type of AGB in general or are a unique case.

As well, the groundwork for dealing with these newer instruments (such as GRAVITY) is being applied to our OITOOLS package and very soon we may start to see the fruits of those efforts. Lastly, we have confirmed the angular size of RZ Ari (Figure 2.3) which has further constrained the mass and other properties of this AGB star.
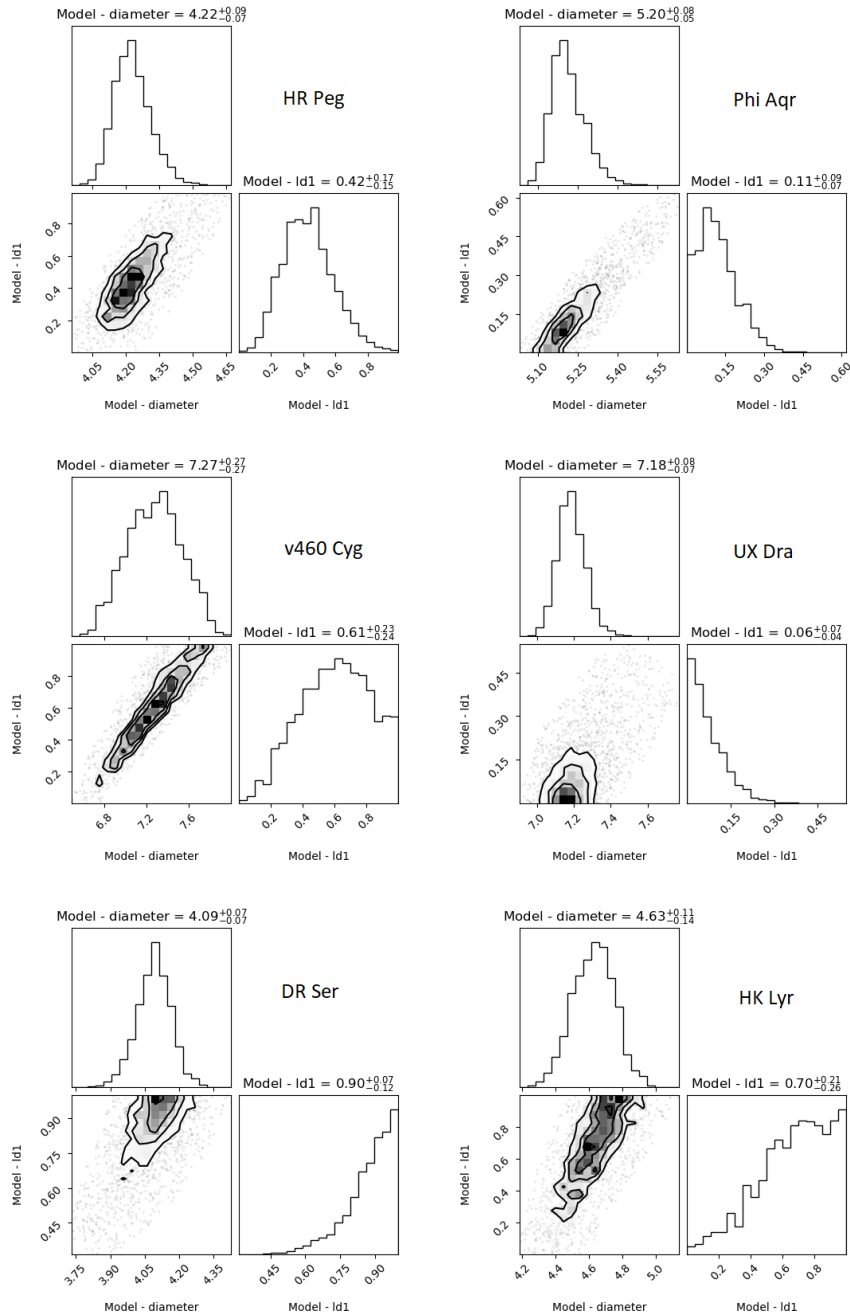
Figure 2.2 Here are the model fits for a selection of our AGB targets. For each star, the corresponding triple-plot is: the upper left plot shows the distribution of diameters fit, the lower right shows the distribution of limb-darkening, and the lower left plot shows the topographical diagram of the two fits. Plots and analysis of the observing data was conducted using our OITOOLS package.
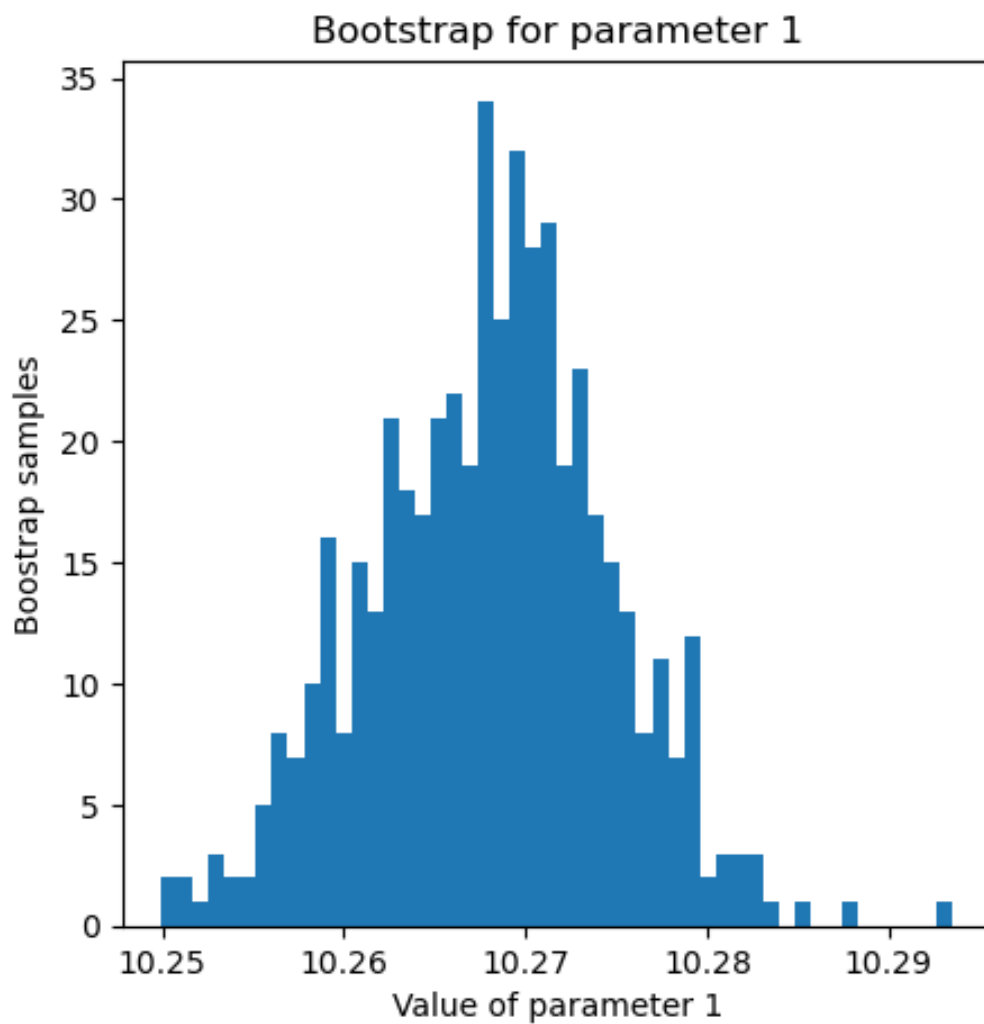
Figure 2.3 Bootstrap fit for the angular size ("parameter 1") of RZ Ari. The mean here corresponds to 10.268 with a standard deviation of 0.0066. These results were shown in part on the paper and poster from Konstantinova-Antova et al. (2021). The bootstrapping and analysis was generated, once again, using our OITOOLS package.
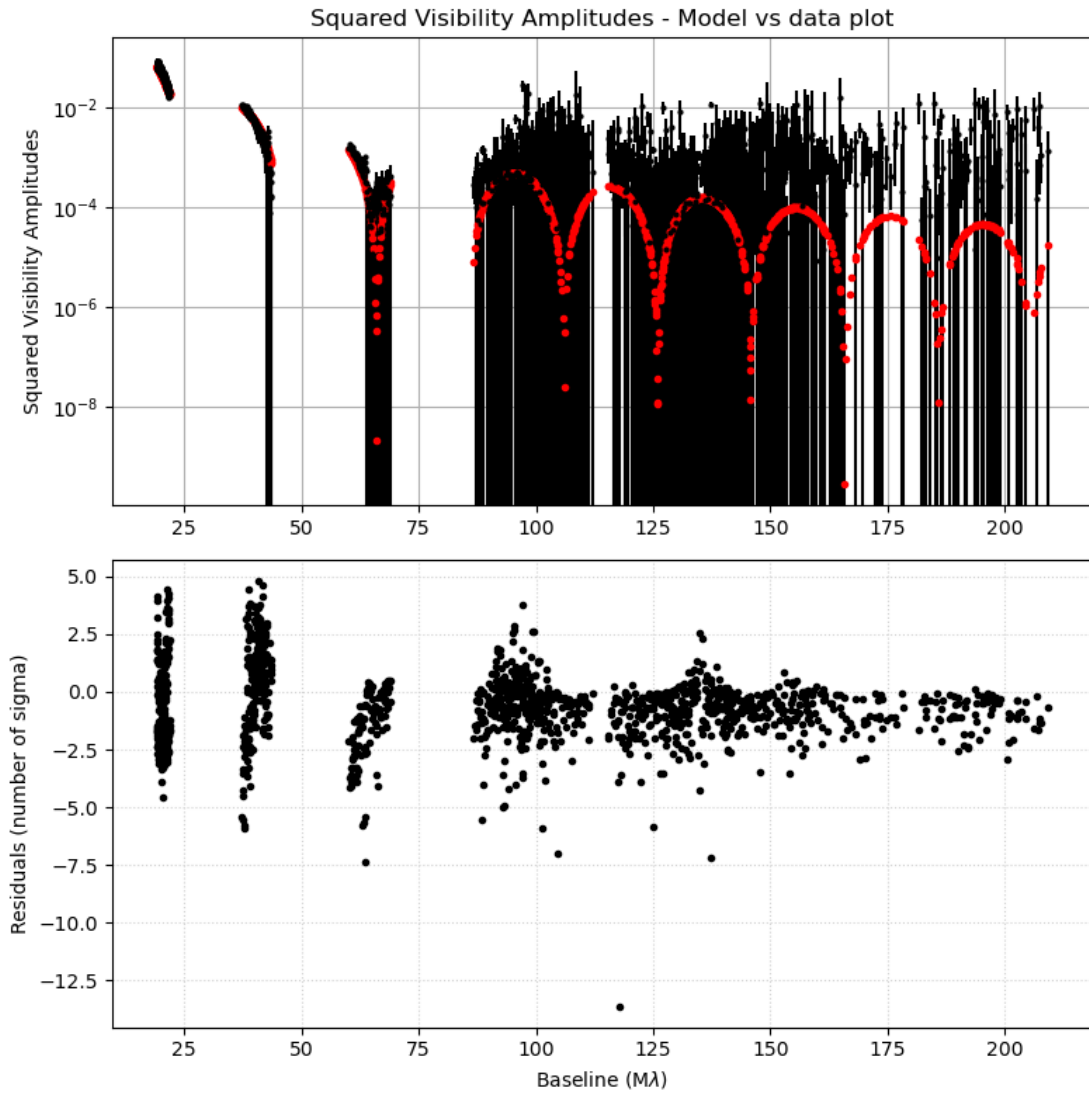
Figure 2.4 Squared Visibility Amplitudes for the model versus the data (red and black, respectively) for RZ Ari. Of note, and as mentioned in Section 2.3.1, the fit to the first lobe (the far left data on the upper plot) is were key information, such as the size of the star (shown in Figure 2.3), is kept.
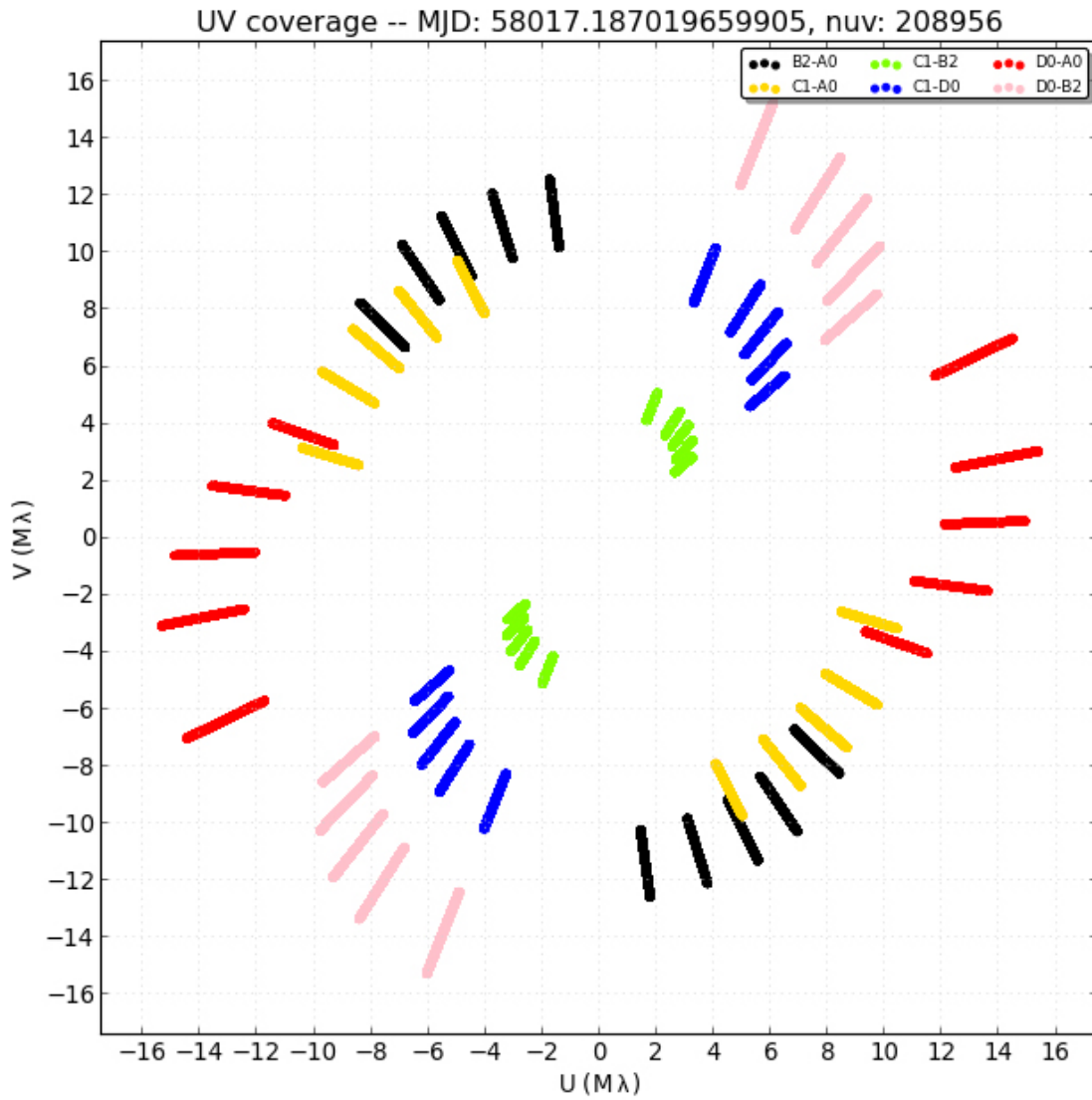
Figure 2.5 Example UV plot for π Gruis.

Chapter 3
DYNAMIC LIGHT CURVE INVERSION WITH ADMM

In this chapter we discuss the process and results of combining LI with ADMM. The breakdown of this chapter is: Section 3.1 discusses the theory and process of combining LI and ADMM, Section 3.2 goes over the production and reconstruction of various simulations (with the results of the reconstructions shown in Section 3.2.4), Sections 3.3 and 3.4 use our LI-ADMM algorithm to reconstruct real-world mission data. Lastly, Section 3.5 reviews the results shown throughout this chapter.

3.1   Combining LI with ADMM

Adapting ADMM into LI involves introducing the Harmon regularization parameters into our solution for x detailed in Equation 1.10; these are implemented essentially as a substitute for our previous transformation matrix, A along with a weighted regularization for spot temperature. The updated equation, for a simple reconstruction with only the TV regularizer, is thus:

$$x_{k+1} = (H^T W Y + \nabla^T (\rho_r z - u)) *$$
$$((H^T W H + \rho_r \nabla^T \nabla) + \lambda C^T (VC))^{-1}$$

$$(3.1)$$

$$\nabla = [\nabla_S^T, \nabla_W^T]$$

$$(3.2)$$

Here, H is the polygon area which corresponds to the area of a given pixel (when multiplied with temperature map this corresponds to a polyflux). W is the inverse-weight per pixel. Y is the observed flux from the star. C and V (Equation 15 in Harmon & Crews (2000)) then are weighting factors and penalty function to bias towards brighter or darker spots. The ∇ parameter here is still a spatial derivative but is specifically a matrix of the transposed "south" and "west" spatial derivatives (Equation 3.2). A compilation of the parameters and variables used in these procedures are shown in Table 3.1.

Table 3.1.   Parameter Description

Parameter	
Parameter	Description
x	Reconstructed image/datacube
y	Corrupted/noisy data
z	ADMM Substitute
μ	Noise/weight
λ	Regularization weight
∇	Spatial derivative
D_T	Temporal derivative
u	Lagrangian operator
H	Polygon Area
W	Square Inverse Flux Error
C, V	Biasing Regularization
i	Inclination
p	Period
T	Temperature
n	Tesselation Level

Note. — Table detailing parameters and variables used for this paper. For our purposes here y, or Y represents the flux data from the light-curve

The equations solving z and u remain the same as before (Eqns. 1.9 and 1.11). Since V depends on x we are limited in our ability to simplify Equation 3.1, otherwise we could pull the denominator for x out of the iterative loop thus speeding up the process.

With these changes, and using the derivatives defined within the Healpix scheme ($\nabla = [\nabla s, \nabla w]^T$) we are able to utilize the basic ADMM structure into reconstructing images via LI. Adding in the mask and temporal regularizers changes the reconstruction equation further and can be easily tracked by adding to the extended Lagrangian equation we defined earlier (Eqn. 1.15). Thus the new iterative equation to solve for x is now:

$$x_{k+1} = (H^T W Y + \nabla^T (\rho_r z - u) + (\rho_m z_m - u_m) + (\rho_t z_t - u_t))*$$
$$(H^T W H + \rho_r \nabla^T \nabla + \lambda C^T (VC))^{-1} \tag{3.3}$$

With the other iterative solutions remaining unchanged.

Combining everything discussed thus far we now have our full reconstruction process. The steps of which are shown in Algorithm 1.

Algorithm 1 An algorithm for performing LI with ADMM

Input light-curve data (flux, error, time) y
Define base parameters i, p, T, n
Define regularization parameters B, λ_{TV}, λ_t, ρ_r, ρ_m, ρ_t
while not converged **do**

 1. Solve x-subproblem (Equation 3.3)

 2. Solve z-subproblems z, z_m, z_t (Equations 1.11, 1.12, 1.16)

 3. Update Lagrangian multipliers u, u_m, u_t, u_{V_t} (Equations 1.9, 1.13, 1.19, 1.20)

 4. Check convergence

   if threshold met **then**
      break
   end if
end while

With this now in hand we have an adaptable way of minimizing the Augmented Lagrangian Method and are able to return a denoised and deblurred reconstruction of the stellar surface from a light curve. This algorithm has been coded and added into our ROTIR

package; for more information on ROTIR, SIMTOI, OITOOLS, and other packages used in our group, I direct the reader to Martinez (2021).

3.2   Simulations

3.2.1   *Making the Simulation*

To confirm the validity of the code, and test for further improvements, we first test the code using generated light-curves with various stellar parameters (Table 3.2) and spot parameters (Tables 3.3 and 3.4) for static and dynamic spot motion, respectively. The simulator works by first building a map of the spotted surface based upon spot parameters and then determining the observable flux by multiplying the surface temperature map by the polygon area for the given stellar parameters. The polygon area is then updated for the next epoch to reflect the new observed face of the star (based upon the period/phase the star is observed at) and the spots change depending on the parameters set. Throughout the process the user has full control over the pixel scheme, tessellation, and various other structures of the map beyond just the spots. Currently the simulator only performs linear changes to a spots radius, position, and temperature but further plans involve more complex degrees of change. There is also the option to produce a random seed of any given number of spots, with or without dynamic changes, within a preset desired range of values; unless otherwise stated our simulations shown here are a curated selection of these random seed productions.

For both the static and dynamic spots, the light-curves are generated with a number of periods equal to N_{Frames} (Table 3.2) with a number of samples equal to N_{Epochs}. A Gaussian distribution is used to apply noise to the the surface map to an adjustable level. Lastly, the tessellation level (resolution) of the surface map is adjustable as well but here is set such that the total pixel number is 3072; increasing or decreasing the tessellation level (and thus the number of pixels) likewise affects the run-time of the program(s).

Table 3.2.   Simulated Star Parameters

Parameter	Static: Sim. 1	Static: Sim. 2	Dynamic: Sim. 3	Dynamic: Sim. 4
Temperature (K)	4518	5452	5094	3589
Inclination (deg.)	53	22	72	109
Period (days)	6.48	3.93	3.13	3.06
N_{Frames}	10	10	30	30
N_{Epochs}	500	500	3000	3000

Note. — Stellar parameter inputs for the shown simulations. Temperature here refers to the average surface temperature of the stellar surface (not including any generated spots, whose parameters are given in Table 3.3 and 3.4). Inclination is the vertical angle of the star to the viewer with 0 degrees being pole (north) on. N_{Frames} and N_{Epochs} refer to the number of rotations of the star and the total number of "observations" respectively. Other parameters, such as limb darkening law(s) coefficients, are included for generating the light curve and performing the reconstruction but are not delved into in this paper.

3.2.2   Static Spots on Rotating Stars

We begin with the simpler test case(s) of a set of stationary spots on a rotating star; the spot parameters used in the simulations shown can be seen in Table 3.3. The lack of dynamic changes means that no variations between periods and provide a good baseline for seeing the effectiveness of the reconstruction. A couple simulations are shown in Figure 3.1 with the surface map and the simulated observed light curve.

As can be seen, depending on the complexity of the spot pattern, the reconstruction does a good job of reacquiring the original simulated surface map.

3.2.3   Dynamic Spots on Rotating Stars

There are two simulations shown in this work (Simulation 3 and 4) that have spots that dynamically change in: size, temperature, and location. The parameters that produced these simulations can again be found in Tables 3.2 and 3.4 with the corresponding light curves being shown in Figure 3.2; these light-curves and our knowledge of the stellar parameters (Table 3.2) will be all we feed to the algorithm later on in Section 3.2.4.

Table 3.3.   Static Spot Parameters

Parameter	Simulation 1	Simulation 2
N_{Spots}	7	7
Latitude (deg.)	(109, 94, 130, 169, 113, 37, 57)	(100, 106, 84, 75, 101, 145, 8)
Longitude (deg.)	(115, 175, 278, 109, 56, 317, 67)	(213, 186, 209, 57, 221, 147, 289)
Temperature (K)	(3983, 3656, 3820, 3322, 3166, 3211, 3443)	(4528, 4611, 4254, 4729, 4245, 4281, 4847)
Radius (deg.)	(22, 36, 38, 8, 36, 28, 9)	(29, 34, 30, 32, 36, 30, 29)

Note. — Table showing input spot parameters for the simulations generated for reconstruction. Figure 3.1 shows the true surfaces, light-curves, and reconstructed surfaces for these two simulations. The stellar parameters for these two simulations are shown in Table 3.2.

Maps for Simulations 3 and 4, detailed in Tables 3.2 and 3.4, can be seen in the left column of Figures 3.7 and 3.8 along with the reconstruction (right column).

3.2.4   *Reconstructing the Simulations*

With the simulations in hand it is now time to start testing the LI with ADMM. The light-curve data is first split into frames, such as one period or half a period. Using the stellar parameters that produced the simulated light-curve we reverse the process and use these values to generate a blank map, the stellar geometry, and flux distribution based on which pixels are visible for a given observation. Of course, a useful test is to reconstruct a simulation with parameters different than those that generated to see what and how things change (Harmon & Crews 2000; Roettenbacher et al. 2013); as this has been tested and studied elsewhere it is not the focus of this paper, however example images can be seen in Figures 3.5, 3.6, and 3.14 for different values of TV weight and assumed inclinations. Inclination, as shown in those figures, is extremely important for reconstructing the correct surface of the star. Once we have the geometry in hand we follow the steps, outlined by Algorithm 1, to iteratively solve for our temporal datacube x. Figure 3.1 shows the reconstructions for non-moving spots, while Figures 3.7, and 3.8 show the reconstruction for a few periods (or
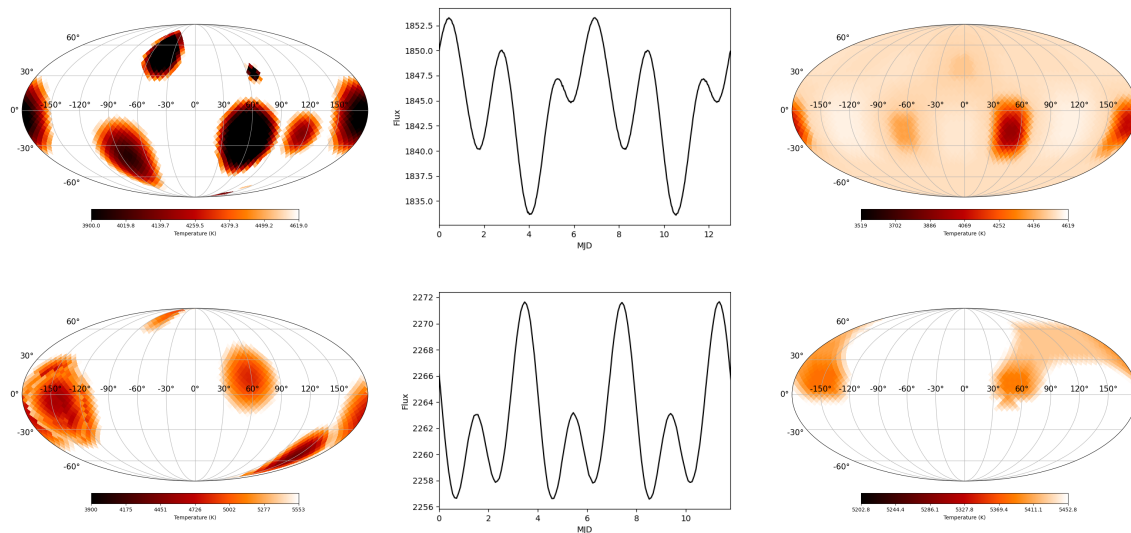
Figure 3.1 Simulations, generated light curves, and reconstructions for the Static Simulations 1 and 2. Listings of the parameters used in the generation of these simulations are shown in Table 3.3, with the stellar parameters shown in Table 3.2. The weights used for the regularizers in the reconstructions are the same as those shown in Table 3.5. As seen in the bottom row, the spots are sometimes superimposed upon each other. Currently the code solves for this by averaging the two temperatures; this is not precisely physical and is a key point for improvement in the next iteration.

frames) of the stars with dynamic spots; all reconstructed periods, for each truth, flat, and random initial guesses, are shown in Appendix A.

The reconstructions shown in these figures are all generated with an initial guess of maps with a flat distribution matching the surface temperature of the simulation. Other options for initializing the code are random or predetermined spot maps. Figure 3.3 shows reconstructions made with these other options (from left to right: truth, true guess, flat guess, and random guess) for Simulation 3; the same figures, for Simulation 4, is shown in Figure 3.4.

Of course it is clear that the spot temperatures do not match on a number of the reconstructions, but by fine tuning the weights of the regularizers one can have greater control over the smoothness and intensity of the spots. Of course with tuning the regularization weights there are risks in under or over-fitting the reconstruction. Examples of a poor recon-

38
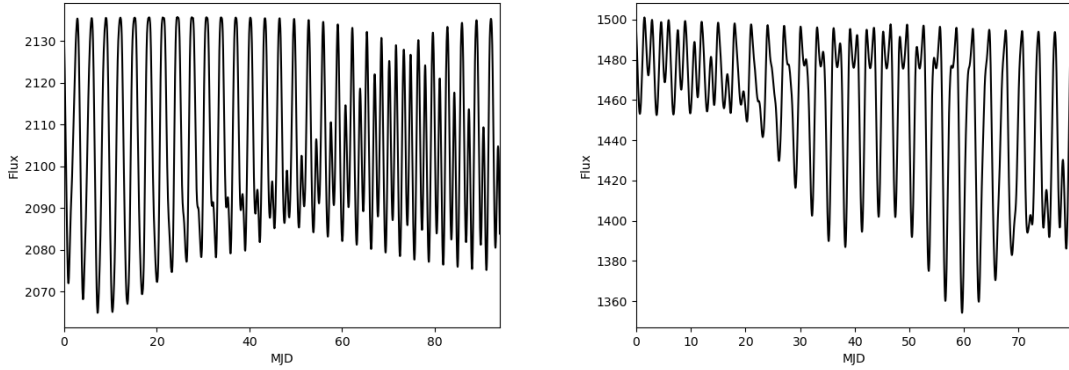
Figure 3.2 Light curves for the Dynamic Simulations 3 and 4. The parameters that generated these light curves can be found in Tables 3.4 and 3.2. The stellar surfaces that made these curves, along with the reconstruction attempts, are shown in Figures 3.7 and 3.8.
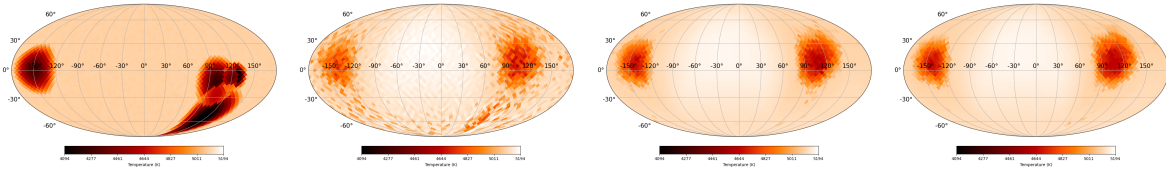
Figure 3.3 In this figure we show the originating surface map (left) and three reconstructions using various initial guesses (noisy-truth, flat, and random respectively) for Simulation 3.

struction, with the weight of the TV parameter turned up or down respectively, are shown in the left and right figures of Figure 3.5. Further differences in reconstruction come down to the critical value input for the inclination. Figure 3.6 shows the results of reconstructing a surface map with various (including the true one) inclinations. Here, it is obvious to see that the inclination one chooses for the reconstruction is an extremely important factor in determining the spot location and pattern. For a similar example using real data, please see Figure 3.14 for reconstructions of TESS data for YZ CMi. It is important to note as well that an inclination of 90° forces all spots to lie on the equator; this is due to the tilt being the factor that allows LI to estimate spot latitude.

As seen in the figures the quality of the reconstruction is greatly hinged upon the complexity of the stellar surface and the inclination at which it is observed. Multiple spots,

39

Table 3.4.   Dynamic Spot Parameters

Parameter	Simulation 3	Simulation 4
N_{Spots}	5	5
Latitude (deg.)	(97, 117, 153, 41, 31)	(137, -7, 110, 112, 186)
Longitude (deg.)	(229, 121, 49, 273, 321)	(352, 39, 33, 172, 356)
Temperature (K)	(3796, 3059, 3135, 3531, 3544)	(2318, 2545, 2321, 2315, 2863)
Radius (deg.)	(28, 5, 23, 26, 41)	(19, 0, 36, 37, 44)
Δ Lat.	(6, 38, 10, 64, 18)	(42, -54, -2, 50, 150)
Δ Long.	(-115, 178, 57, -170, 153)	(128, -119, -139, 142, 146)
Δ Temp.	(-202, 363, -400, -360, -655)	(-447, -30, 139, -236, -47)
Δ R	(4, -28, -2, 10, 20)	(1.8, -21, 18, 2.7, 9.5)

Note. — Table showing input spot parameters for the dynamic simulations generated for reconstruction. Here the Δ parameters denote the total change (from first to last frame) for that spot with linear steps between. Figure 3.2 show the corresponding light curves and Figures 3.7 and 3.8 show the ADMM reconstructions.
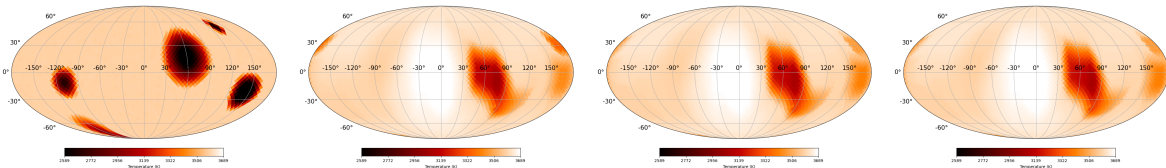
Figure 3.4 In this figure we show the originating surface map (left) and three reconstructions using various initial guesses (noisy-truth, flat, and random respectively) for Simulation 4.

close together, may bleed into a single reconstructed spot as can be seen in many of the reconstructions (a good example being Figure 3.8). As well, as with LI in general, the assumed and simulated inclination of the star is a massive factor in the reconstruction efforts. Looking further at the comparison between Figures 3.6 and 3.14 we can see that depending on which angle we view the star the number, location, and intensity of spots can vary; all due to the polyflux and how the geometry determines which pixels are visible and carry the most weight.

There is of course room for improvement to round out the robust nature of the simulations and allow non-linear changes to size, temperature, and location of the spot as a function of
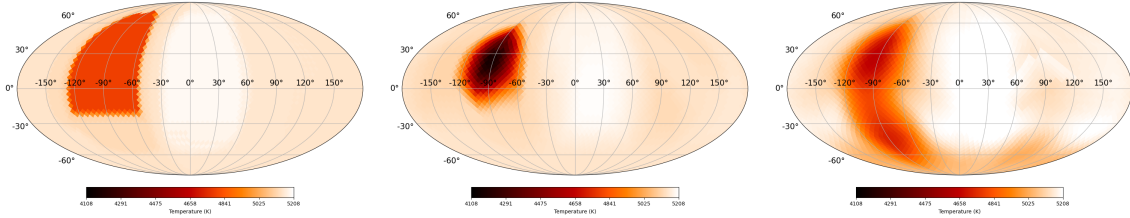
Figure 3.5 Here is shown example reconstructions of the same stellar surface given different regularization weights for TV. The figures weights, starting on the left, are $\lambda_{TV} = 0.138$, $\lambda_{TV} = 0.00138$, and $\lambda_{TV} = 0.0000138$. As can be seen there are increasingly exaggerated changes as the TV is tuned higher or lower. And, while the right-most (lower TV weight) image may more closely resemble the truth image (Figure 3.8, upper left image) in terms of the locating the spot on the lower hemisphere it comes at the cost of the spot's intensity.
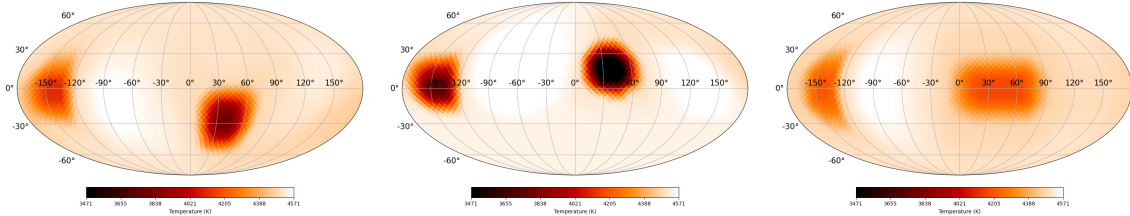
Figure 3.6 Here is shown example reconstructions of a random stellar surface, given different inclinations, to show how inclination changes the response of the reconstructor. The figures inclinations, starting on the left, are $i = 122$ (the true), $i = 35$, and $i = 90$.

the time/epoch being simulated; as well we would like to add non circular geometries. Steps towards this end are detailed more in the Future Work section (Section 5.2). However, even without these upgrades the simulator is complete enough for making linear, time-variable, surface maps and their corresponding light-curve.

3.3   Application to KIC 5110407

In this section we apply our LI-ADMM code to the same target data (KIC 5110407) from Kepler as reconstructed by Roettenbacher et al. (2013) (who used pioneered by Harmon & Crews) for comparison and proof using real data. Initial parameters and regularizers are found in Table 3.5 and the light curve shown in Figure 3.9. For our purposes here we took

Table 3.5.   KIC 5110407 Stellar Parameters

Parameter	Value
Temperature (K)	5200
Inclination (deg.)	60
Period (days)	3.4693
Limb Darkening Coefficients (e,f)	(0.7248,0.1941)
λ_{TV}	$1e^{-3}$
$\lambda_{temporal}$	$1e^{-3}$
ρ_{mask}	$1e^{-5}$
$\rho_{spatial}$	$1e^{-2}$
$\rho_{temporal}$	$1e^{-3}$
λ_B	$1e^{-3}$

Note. — Stellar parameters used in the reconstruction of KIC 5110407. Limb darkening law used is the logarithmic law with coefficients (e,f) for the *Kepler* bandpass (Roettenbacher et al. 2013; Claret & Bloemen 2011). Included as well are the regularization parameters used for the reconstructions.

a look at 26 rotations of the star and split it into 52 frames (each half a period in length). These half rotations were then split, analyzed with the code, and a reconstruction built of all epochs concurrently (thanks again to the temporal regularization). The full reconstruction, of all 52 epochs, can be seen in Figures A.9 and A.10.

Figure 3.10 shows the reconstruction obtained by our code with the aforementioned parameters. Here we see our method matches closely the reconstruction performed by Roettenbacher and provides a real-data proof of concept for our algorithm. For further comparison, Figure 3.11 shows the same light curve reconstructed with the OptimPak package (Thiebaut 2014). Once more, differences in intensity aside, we see strong agreement in the spot patterns shown. The full OptimPak reconstructions are shown in Figures A.11 and A.12. OptimPak, again, being another optimization library; further work and discussion by the author can be found at Thiebaut (2002).

3.4 Application to TIC 266744225

TIC 266744225, or YZ CMi, is a red dwarf (M4.0Ve C) in the Canis Minoris constellation that was examined by the Transiting Exoplanet Survey Satellite (TESS). We attempt to reconstruct YZ CMi using our algorithm here to further show its applicability; the light curve for the star visible in Figure 3.12. The stellar parameters used for this reconstruction are: $T_{eff} = 3181K$, $period = 2.8days$ (Maehara et al. 2021), with the inclination being tested with 60°. The light-curve here was split into a number of frames with lengths equal to the period of the star. Reconstruction parameters used are the same as those for KIC 5110407, shown in Table 3.5 unless otherwise stated. As well, flare-like signatures from the light-curve are not removed.

The results of the reconstruction, with the aforementioned parameters, are shown in Figure 3.13. As mentioned in an earlier section, for an example reconstructed frame of YZ CMi with different assumed inclinations see Figure 3.14. There we can again see the importance that inclination has on the reconstruction one receives.

3.5 Discussion of LI Results

In this chapter, we have shown a new algorithm for performing LI that not only matches the results of other methods but will also prove to be a grand step towards better and more efficient ones. ADMM provides adaptable and efficient LI reconstructions as tested on simulations (Figures 3.1, 3.7, and 3.8) and observational data from both *Kepler* and *TESS* missions (Figures 3.10 and 3.13).

We also explore the limitations and considerations with LI and ADMM in general. Figures 3.6 and 3.14 display the importance of inclination when performing reconstructions. Figure 3.5 shows the power and control that the weights of the regularizers have over the reconstruction. And Figure 3.11 shows a comparison of our reconstructor with other existing packages.

Lastly, as mentioned before, we show in this chapter the robust (and every improving) light-curve simulator. The open-source code allows the user to input spots upon a stellar surface and, with full control over the star and spot parameters (Tables 3.2, 3.3, and 3.4), allow the system to evolve; producing not only the resulting light-curve information but maps of the stellar surface for each epoch. We aim to continue evolving this simulator to perform more complex (non-linear) changes between epochs, different geometries (of spots and stars), and more.

The results detailed in this chapter are soon to be submitted for publication (Abbott et al. in prep A). This paper will report on the items summarized here along with further comparisons, simulations, and analysis.
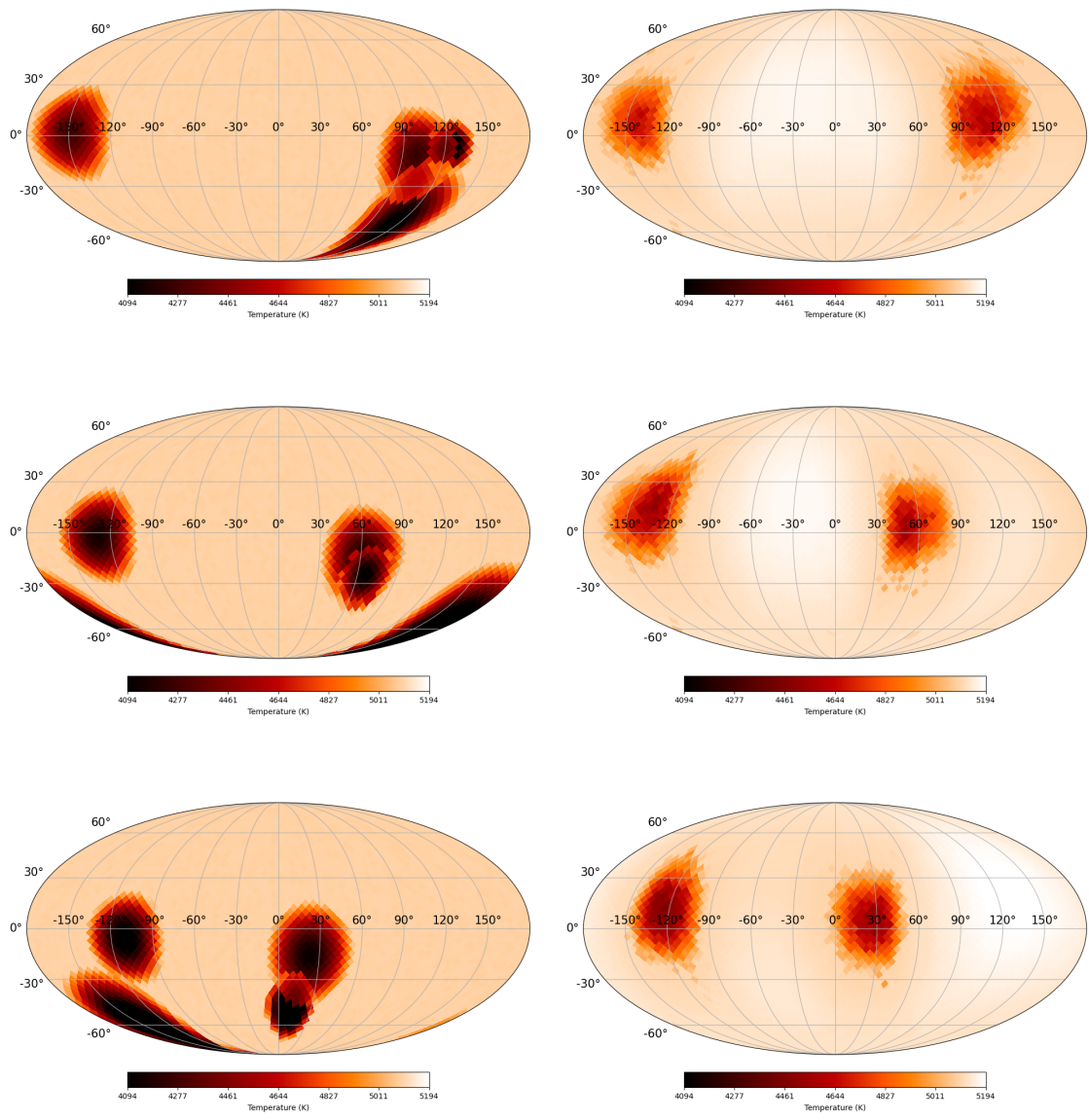
Figure 3.7 This figure shows the results of the Simulation 3 and its reconstruction with our ADMM-LI code. This simulation uses a flat image (filled with the average surface temperature, XXXX K. The full reconstruction of all the epochs are shown in Figure A.3. For reconstructions made with other initial guesses, such as the truth and random images, see Figures A.2 and A.4 respectively.
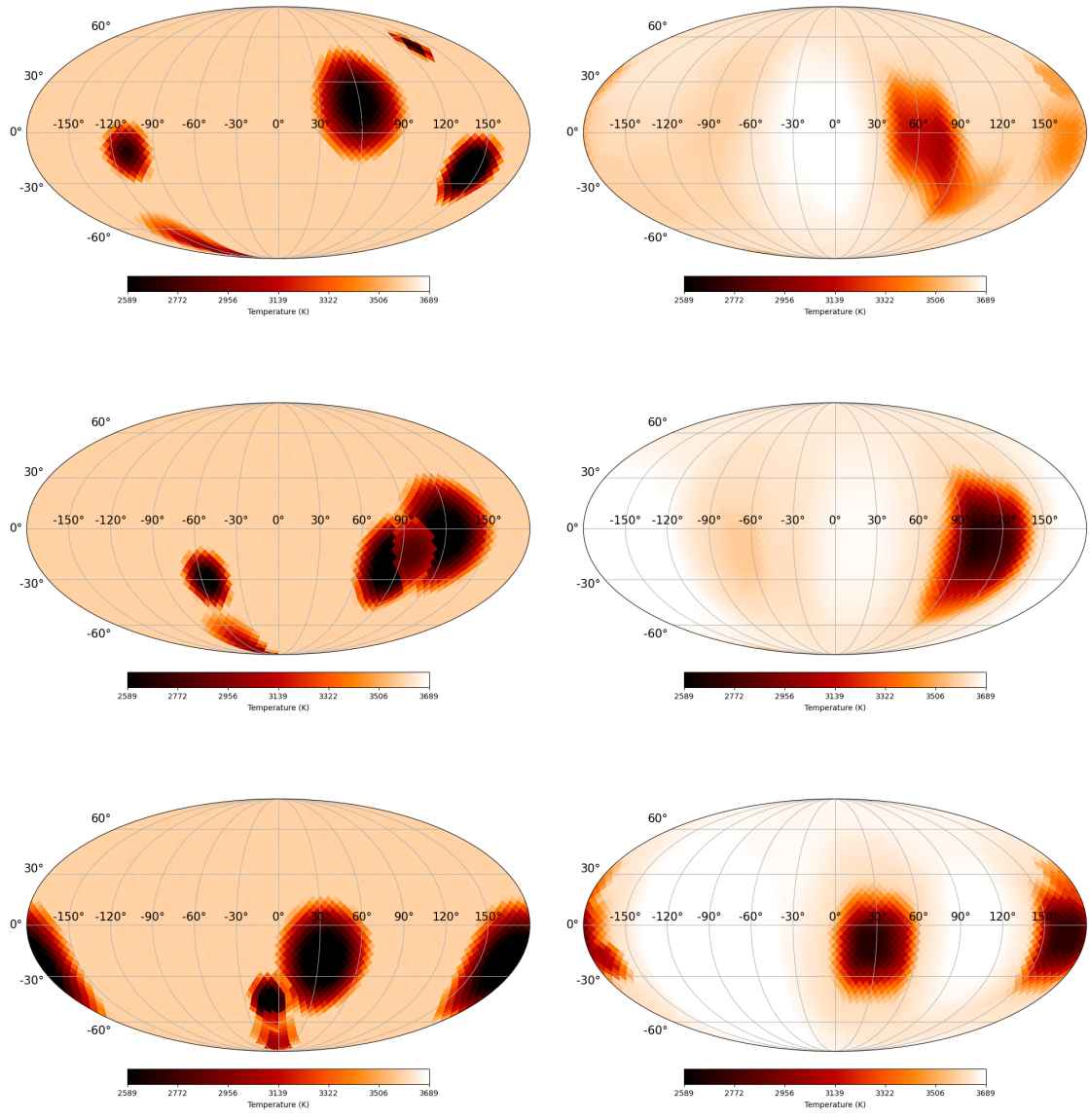
Figure 3.8 Reconstruction of Simulation 4 in the same scheme, and initial guess setup, as Figure 3.7. For full reconstructions of the truth, flat, and random initial guesses see Figures A.6, A.7 and A.8 respectively.
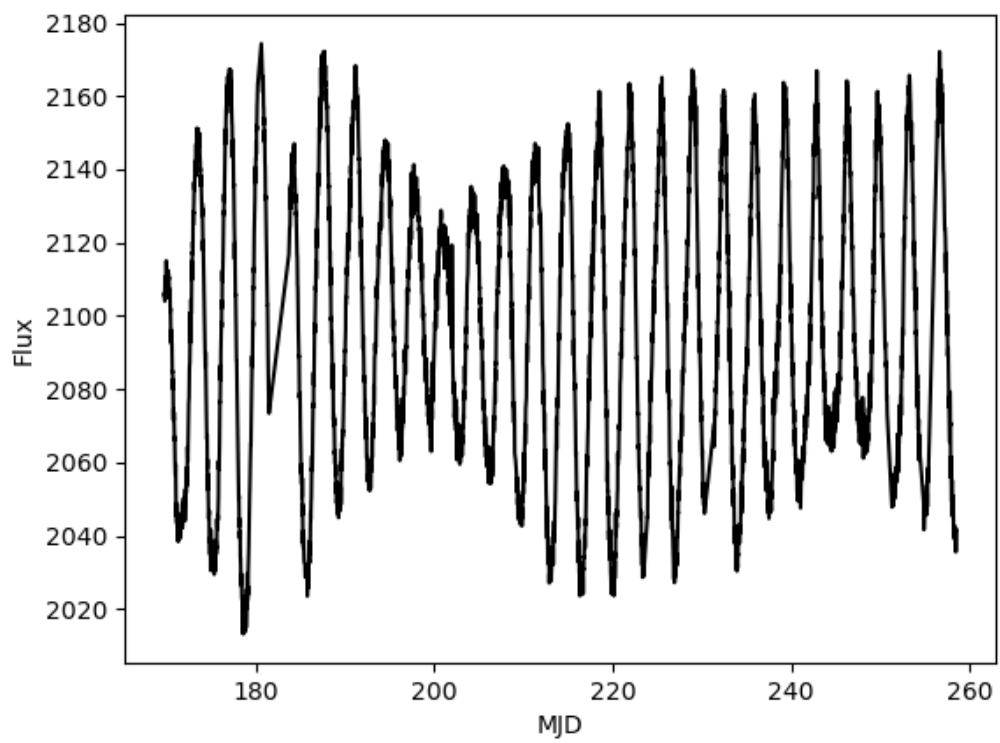
Figure 3.9 Shown here is the light-curve for KIC 5110407.
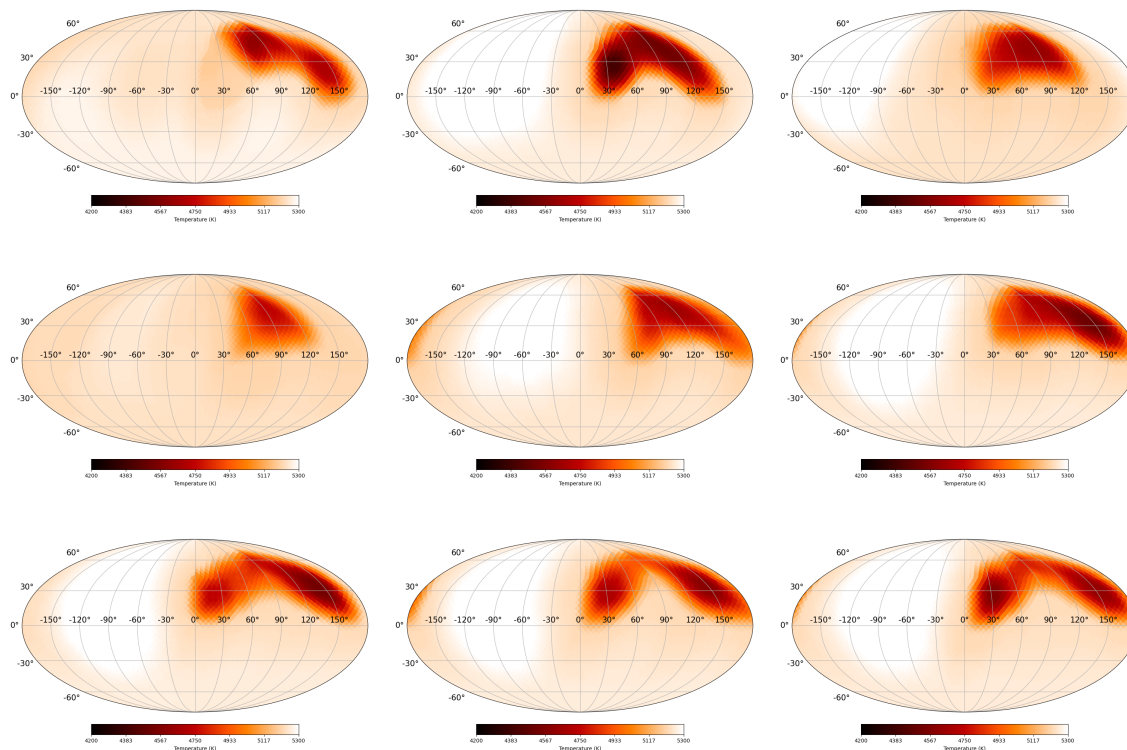
Figure 3.10 Image showing nine of the ADMM reconstructions (sequentially from left to right, and top to bottom row) for KIC 5110407. Comparisons to the OptimPack image restoration method (included with OITOOLS) is shown in Figure 3.11. All 52 images for the reconstruction are shown in Figures A.9 and A.10.
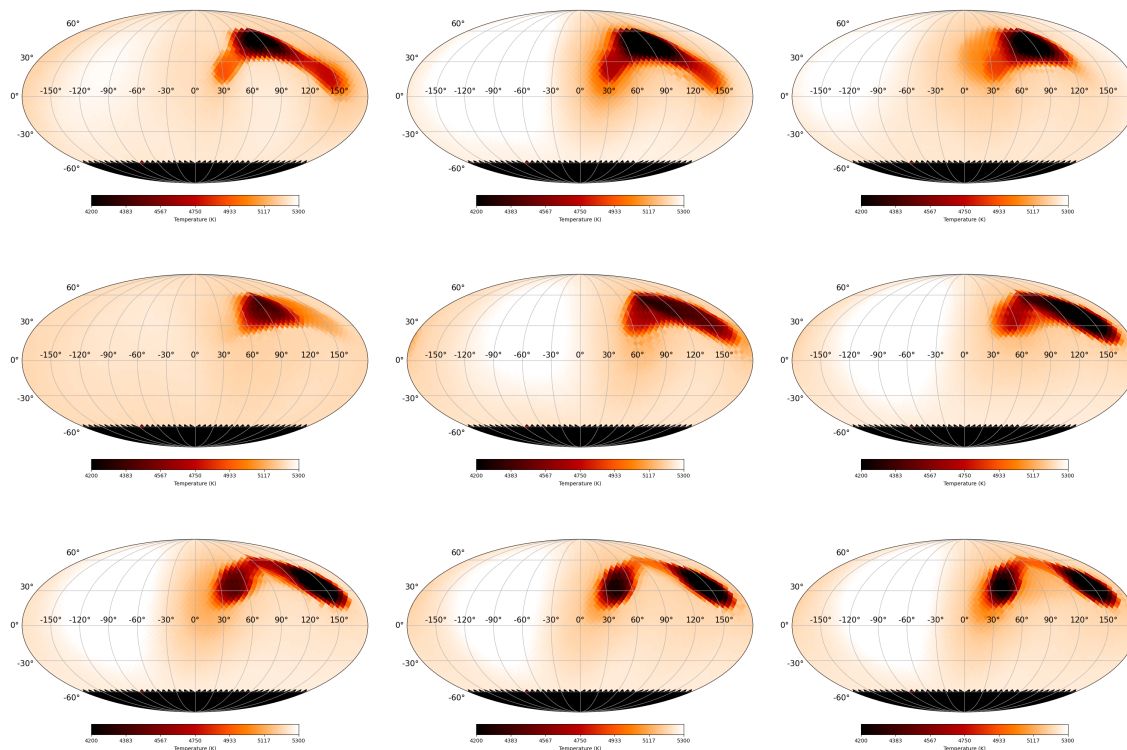
Figure 3.11 Image showing nine of the reconstructions (sequentially from left to right, and top to bottom row) for KIC 5110407. These images were generated using the OptimPack library. The epochs shown here are the same as those shown in Figure 3.10. All 52 OptimPak reconstructions are shown in Figures A.11 and A.12.
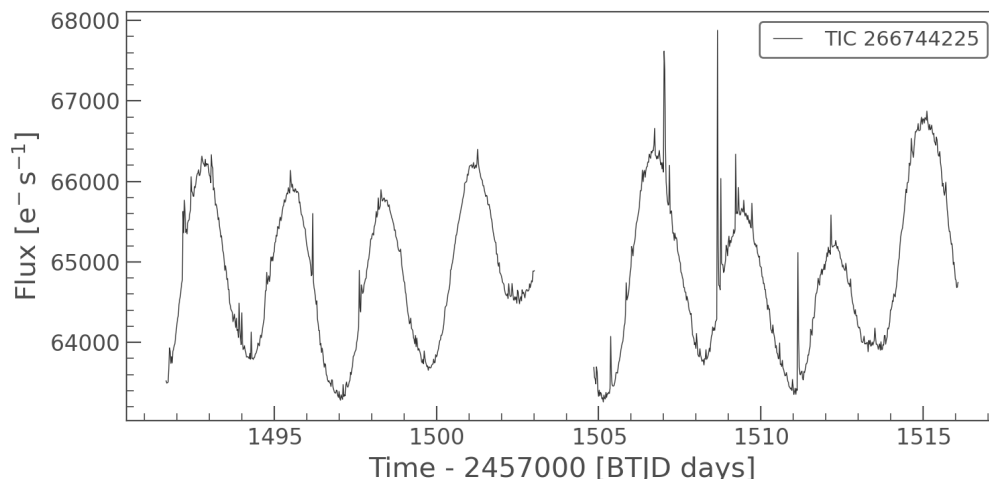
Figure 3.12 Shown here is the light-curve for TIC 266744225. Plotted using the LightKurve software provided by TESS. This data covers nine rotational periods of this star; one of the rotations falling within the gap in the data.
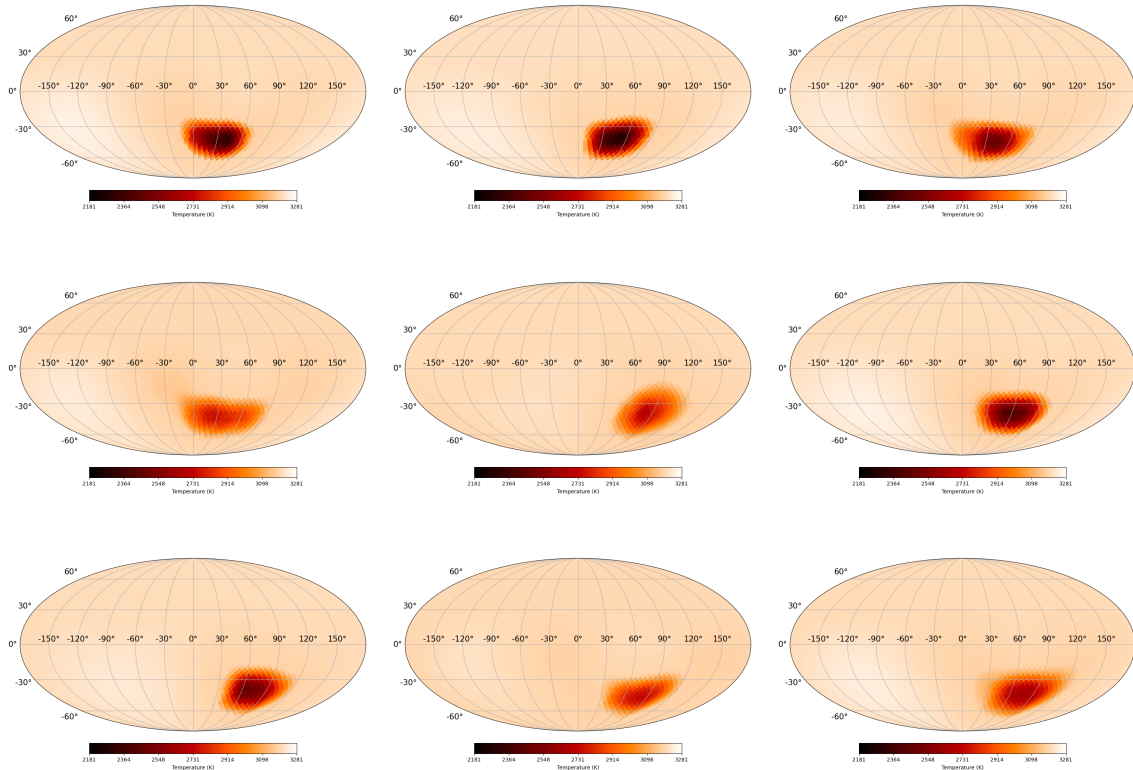
Figure 3.13 This figure shows the results of the reconstruction of YZ CMi from TESS data using the ADMM-LI code. Stellar parameters used in this reconstruction are: $T_{eff} = 3181K$, period $p = 2.8 days$, and $i = 145°$. Other parameters, if not otherwise mentioned, are the same as those shown in Table 3.5.
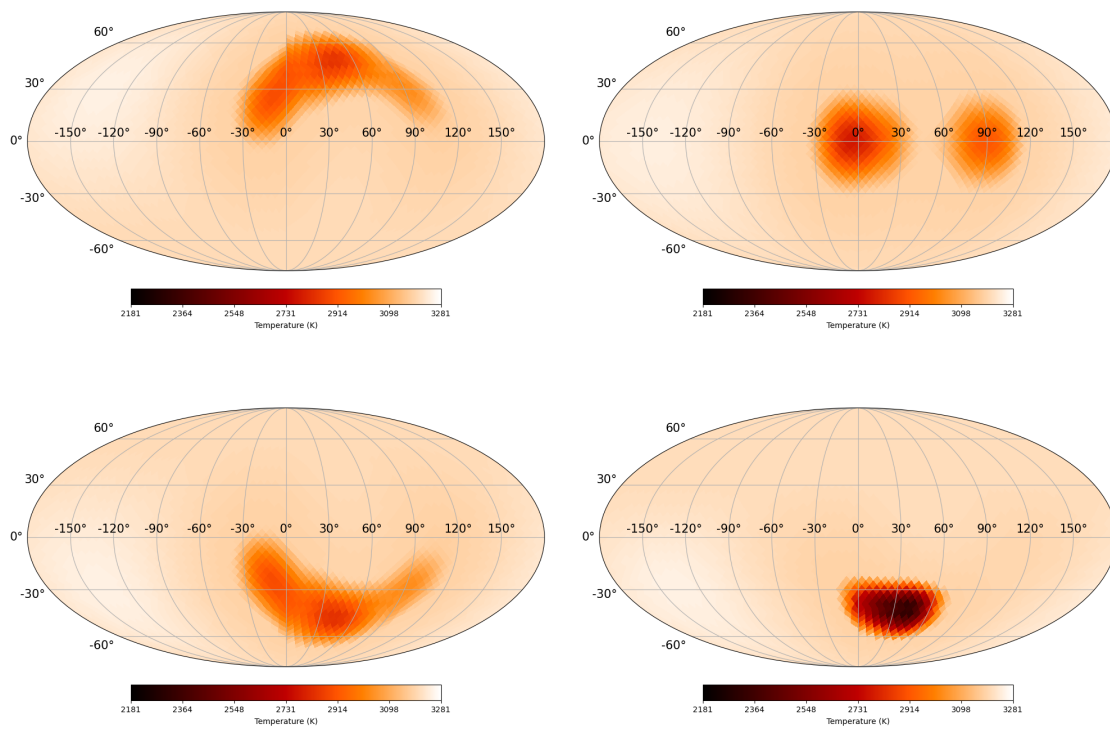
Figure 3.14 Reconstructions of YZ CMi given different inclinations. The inclinations used here, from left to right (starting on the first column), are $i = 60°$, $i = 90°$, $i = 120°$, and $i = 145°$

Chapter 4
INSTRUMENTATION

While computer simulations, even those shown in this manuscript (such as Section 3.2), can be extremely useful, it is impossible to ignore the benefits of doing real, physical, simulations with directly observable results. With instruments we can test real world scenarios, with photons and induced aberrations, all in a controlled environment. The breakdown of this chapter is as follows: Section 4.1 covers the design of our atmospheric turbulence simulator, Section 4.2 covers other instruments being built in our lab, and Section 4.3 goes over a discussion/summary of the results shown in this chapter.

4.1   ARES Atmospheric Simulator

The goals and capabilities of the Advanced Reconnaissance of Earth-orbiting Satellites (ARES) instrument are as varied as the number of parts on the table and go far and beyond its name. Its originating purpose was to be an atmospheric turbulence simulator for analysing the effects of light from some source travelling upward and/or downward through the atmosphere, and this is the context of which the instrument will be first described; additional uses and potentials of ARES is detailed in Section 4.1.3.

ARES is divided into two optical paths or "legs": the Downlink and the Uplink. A diagram of the instrument is shown in Figure 4.1 with a more thorough overview of the optical set up detailed in Section 4.1.1. ARES is designed such that each of the legs may be used separately or combined in various ways depending on what the user wishes to simulate. For our goal, we use both legs to simulate light coming down from a target, such as a satellite, through the atmosphere (Downlink) and then sending a laser back up through the atmosphere, pre-correcting it with an added DM at the start to minimize the degradation of the information sent (Uplink).
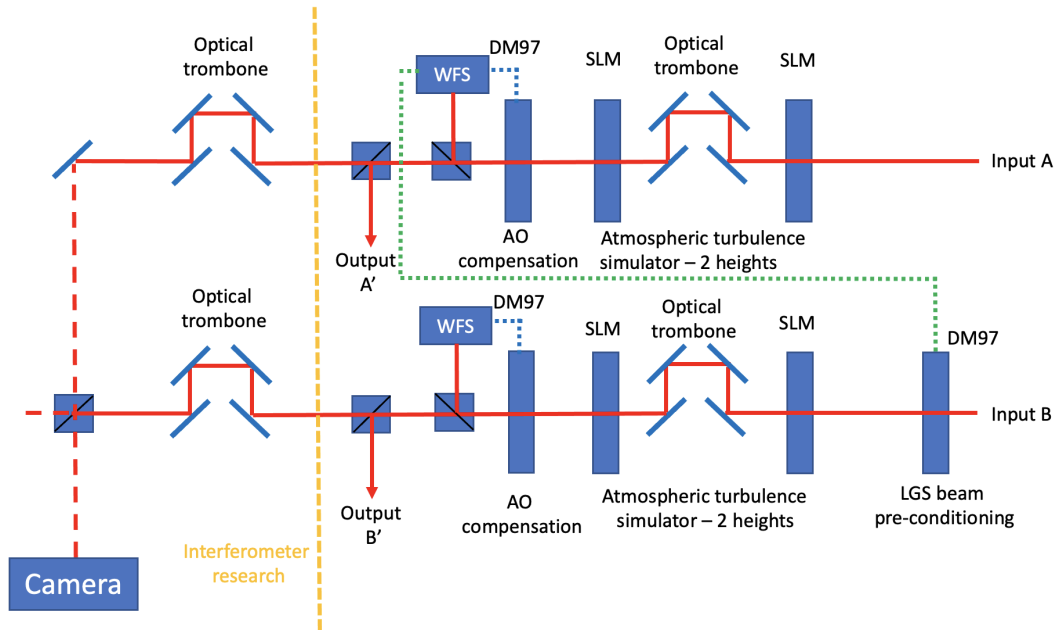
Figure 4.1 Here is the simplified schematic of the ARES design. Input A is what we call the "Downlink" and Input B is the "Uplink". Of special note is that Input A and B communicate to each other via the WFS of Input A being used to pre-correct the first DM on Input B.

4.1.1 *Optical Setup and the Zero-Order Diffraction Spot*

The Downlink simulates light coming from some object at infinity which then passes through two layers of atmosphere (with the separation between the layers at a programmable simulated heights) where it is observed, and the wavefront distortions recorded by a Shack-Hartman WFS. In our instrument, the atmospheric layers are simulated via the SLMs loaded with phase screens of the desired turbulence (Sections 1.4.1 and 1.4.3) and the observer can be thought of as the WFS towards the end. A camera, another instrument, and an AO system are all further options to observe and utilize the effects of the simulated atmospheric turbulence. Specifically, one intent of the AO system is to use it with simulating AO compensated speckle imaging.

The key component of setting the height difference between the layers of the simulations is the optical trombone, made possible with a Zaber stage. A Zaber stage is a motorized linear translation stage with steps of 2.5μm with a farthest travel distance of $7.5cm$. The

Zaber works by changing the distance between the two SLMs to simulate various levels of propagation and thus various levels of simulated height differences. Once the distance between the SLMs is changed from the default 4F system (which relays the pupil from one SLM to the other; Section 1.4.4) propagation effects begin to appear. The effects of the propagation increasing as the distance between the SLMs increases.

$$F_n = \frac{D_s^2}{\lambda z_s} = \frac{D_A^2}{\lambda z_A} \tag{4.1}$$

Here, λ is the wavelength of the light, D_s and D_A are the aperture diameters (the simulated size we want and the actual aperture size, respectively) and z_s and z_A the corresponding propagation distances. The Zaber stage has a total available length of 7.5 cm (for a total variation of 0-15cm from the 4F distance), using Equation 4.1 we see that the simulated propagation distance is proportional to the squared ratio of the physical and simulated aperture sizes. Therefore, as an example, we can see that for D_s=3.6m and D_A=0.01m, we can simulate a propagation range of up to 19.4 km.

For the Uplink path the system is mostly just a reversed version of the Downlink: SLMs for simulating atmospheric turbulence and an optical trombone to set the distance between the two layers in the simulation. Essentially, all one need do for a schematic of the Uplink is reverse the beam direction of the Downlink. The main goal of the Uplink is to simulate a return beam traveling back up through the same, or rather slightly different, atmosphere that the Downlink simulates. The difference in phase screens should be seen most in the higher layer, depending on the coherence time and other conditions simulated. That is to say that, wind speeds and motion of the target depending, the atmosphere between the source and the instrument on the ground will have the greater change in the uppermost level of the atmosphere due to having a larger angular displacement compared to the lower/ground levels.

The key difference between the two legs is (in the Uplink) the presence of a DM prior to the beam interacting with the SLMs. This DM allows us to pre-correct the wavefront of

the Uplink beam based upon the WFS data from the Downlink. Of course, the wavefront will not be the same as the atmosphere being simulated is slightly different. However, the pre-correcting of the beam should mean that the observed beam after both SLMs is closer to a "clean" (un-aberrated) beam. The result(s) of our experiments, thus far, with the ARES instrument are discussed further in Section 4.1.2.

An important component in both legs of the system is the Half Wave Plate (HWP) set into each leg to mitigate what is known as the Zero Order Diffraction Spot (ZODS). The ZODS, visible in Figure 4.3 around $D/r_0 = 40$, is due to light that is not modulated by the pixels on the SLM: e.g., the light reflected from between the pixels. It becomes increasingly visible as the D/r_0 rises because the modulated light from the SLMs is being diffused more and more through additional spots; the number of spots going as $N_{speckles} \sim (D/r_0)^2$. This means to test high turbulent atmospheres and fully trust the results of our simulations we have to mitigate or remove the ZODS as much as possible. We do this by installing a HWP and rotating the polarization of the beam until the resulting light off the SLM is at a minimum and using a linear polarizer as an analyzer. Other methods for mitigating the ZODS include: multiplexing a fresnel lens on the SLM as one of the relay lenses, defocus (Figure 4.2), or a blazed grating; all these though have their own side-effects and thus we go with the polarization and defocus approaches here.

4.1.2 *ARES: Results*

The ARES project is very much an ongoing endeavor and collaborative effort with the NASA Jet Propulsion Laboratory (JPL). So far in this chapter we have laid out the progress and plans for our extensive simulator. The current main results of the experiment lie in its ability to recreate recognizable PSFs and correct these aberrations with an included AO system; both detailed in the following paragraph. More tests, simulations, and results continue to pour in each day, the results of these (and more) experiments are to be summarized in an upcoming paper and presentation (Abbott et al. 2022).

No defocus   With defocus   Synthetic
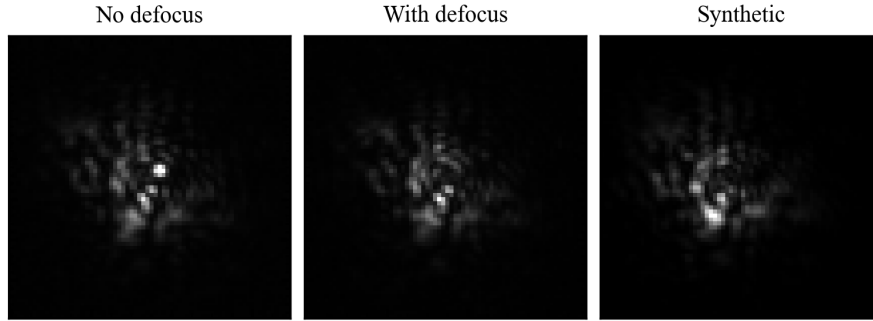
Figure 4.2 This figure shows the removal of the ZODS by using the defocus approach. The image on the left has the ZODS, while in the central image the ZODS is out of focus and can't be seen. The image on the right is the computed synthetic PSF for the phase screen applied to the SLM.

For PSFs, to realize high levels of D/r_0 the phase wraps produced on the SLMs are densely packed and, as the density increases, can lead to information being lost. A comparison between the predicted PSFs for the wavefront applied to the SLM, and the measured PSFs from the simulator, can be seen in Figure 4.3. Most of these show great agreement between the simulated and observed PSFs, the biggest difference between the PSFs at $D/r_0 > 30$ is the presence of the ZODS (again, showing the importance in removing it). However, when accounting for the ZODS (and other rotational and scale differences) the PSFs produced by our system are beyond recognizable as we found them to be accurate to greater than 90% agreement between the observed and simulated PSFs. This was determined when we performed a Structural Similarity Index Measure (SSIM), a method of comparing the similarity between two images, for our simulated and observed PSFs; the results of which are shown in Figure 4.4.
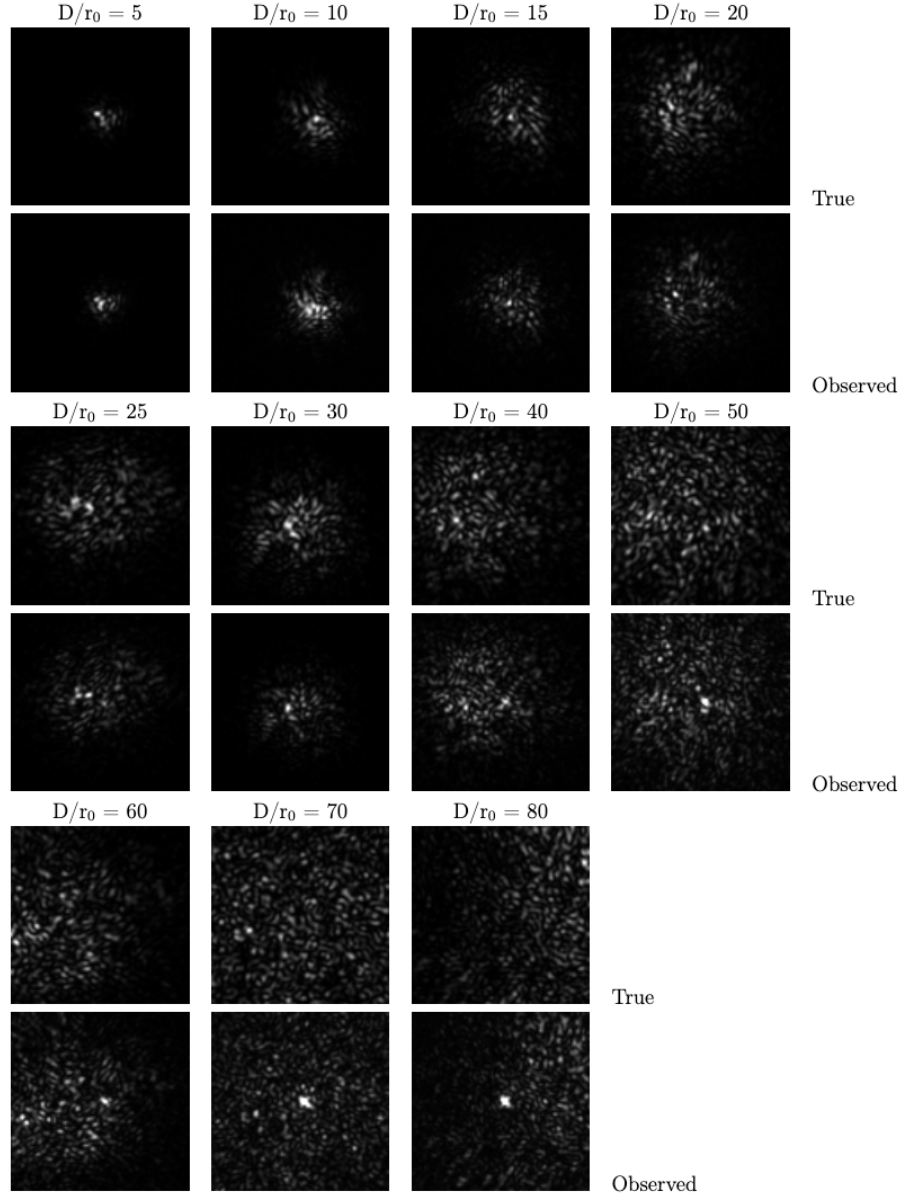
Figure 4.3 This figure shows the results of the PSFs produced by each SLM in the ARES turbulence simulator over a wide range of atmospheric turbulence conditions. The first, third, and fifth rows of images show the expected PSFs determined from numerical simulations. The second, fourth, and sixth rows show the corresponding PSFs generated by ARES. All images are on a linear scale. A zero-order diffraction spot (ZODS) can be seen in the centers of the images for $D/r_0 > 40$. This spot is minimized through polarization control (see the HWP in Figure 4.1). Note, there is a difference in magnification between the true and observed images. When recording the image sequences, we adjusted the brightness of the source for each exposure so as to fill the camera's dynamic range.
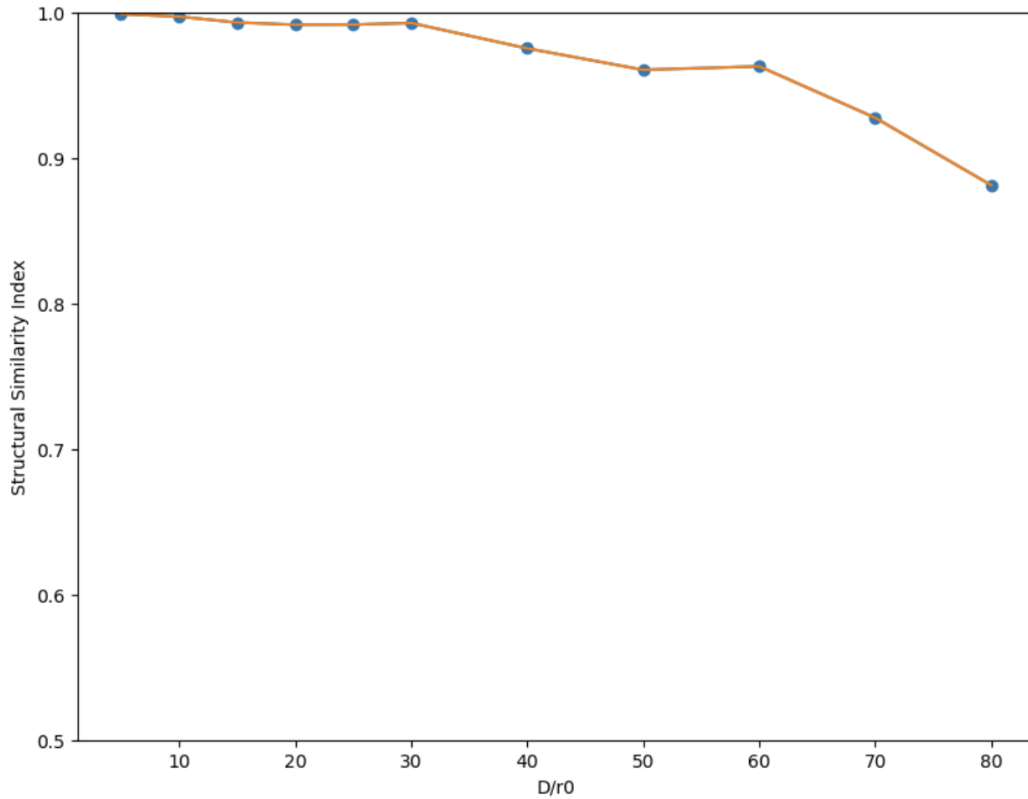
Figure 4.4 This figure shows the Structural Similarity Index Measure (SSIM) comparing our simulated versus observed PSFs (Figure 4.3) for a wide range of D/r0. Here, a 1.0 means 100% agreement between the simulated and observed images and a 0.0 would mean there is none. As can be seen there is a greater than 90 percent agreement between a wide range of our simulated PSFs.

Furthermore, we have the option of correcting these aberrations through the use of our DMs and WFSs synced together to form an AO loop. Example results of AO compensation are shown in Figure 4.5. The ZODS begins to dominate the AO systems attempts to correct the system as the D/r_0 continues to increase; further emphasising the importance of removing/minimizing the ZODS as much as possible.
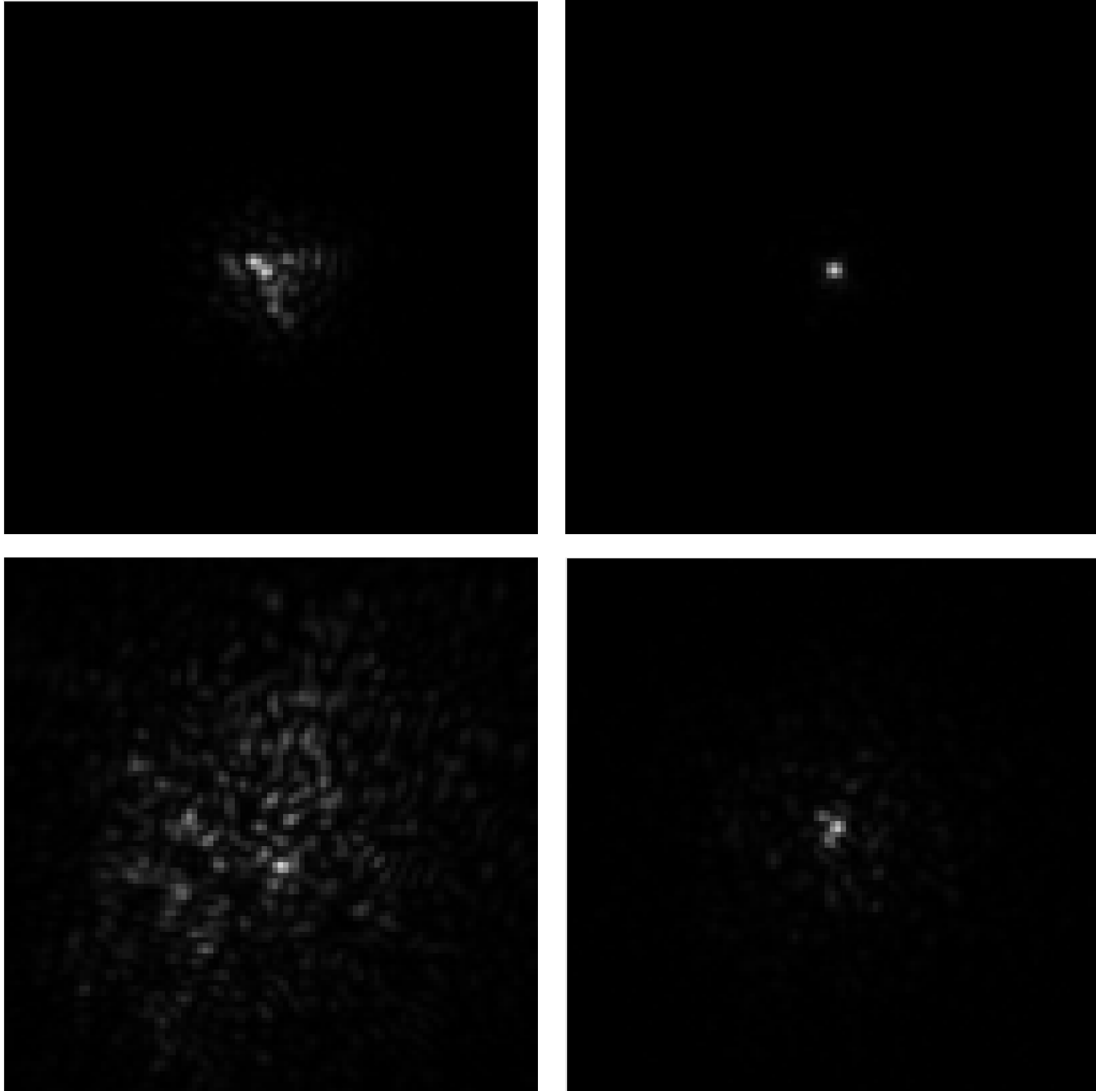
Figure 4.5 PSFs generated from two phase screens, co-located in the entrance aperture, without (left column) and with AO compensation (right column). The turbulence simulated is $D/r_0 = 7$ (top row) and 30 (bottom row).

4.1.3   *Further Applications*

One of the main draws of the ARES system is its extreme adaptability. Nearly every component on the bench is installed with a Kinematic Base (KB) that allow for quick and repeatable rearranging and removal. So, with minimal effort, one can reorganize the system as necessary for whatever function might be needed, such as:

- Interferometric techniques: recombining the legs with the same path length allows simulating interferometric imaging through the atmosphere. An early version of this was explored in our work with Martinez et al. (2021).

- Volume turbulence: adding more SLMs to the path (we have 6 total) to add more and more layers to the simulation; double passes can bring this total to 12 layers. Can do horizontal beam propagation as well, with nine layers possible (one for each SLM, or more with a double pass).

- More complex targets: the instrument to be previewed in the following section (Section 4.2.1) can be put in to allow non-point source objects.

- Testing and analyzing the affects of anisoplantic imaging (imaging through wide field of view); initial results of which are shown in Figure 4.6.

- Future proof: any future project can benefit by being plugged in at the end of a leg (or multiple) and have a clean beam for testing or have the option of simulating various levels of atmospheric turbulence with or without AO compensation.

All these, and more yet undreamed of, will allow ARES to fulfill its original purposes and be the basis for future instrumental breakthroughs within the astronomical community and Georgia State University for the scientists of tomorrow.

4.2 Other Project Designs

Although they currently sit in various levels of completion, each of the following instruments are currently undergoing development in our lab. At least one iteration of each has been installed/attempted with further evolution as we learn and discover what works and what doesn't. Although not given its own section, an important instrument we have just begun installing is a polychromatic simulator. This will allow us to create more complex and realistic objects/sources for testing through ARES and other future instruments. This, in

its current design, is making use of our larger DM241's for greater control and dynamic range.

4.2.1 *Object Generator*

The object generator (ObGen), is a device with two versions: a simplistic and an extended. The simplistic version, shown in Figure 4.7, takes the current entrance pupil of the ARES system (or any other instrument) and puts in an off-axis secondary source. This allows for testing cases such as for binary star systems. As well, we can use this ObGen to measure high-contrast differences, tuning the intensities of the lasers to be simulate bright and fainter targets (such as for detecting exoplanets or other faint companions).
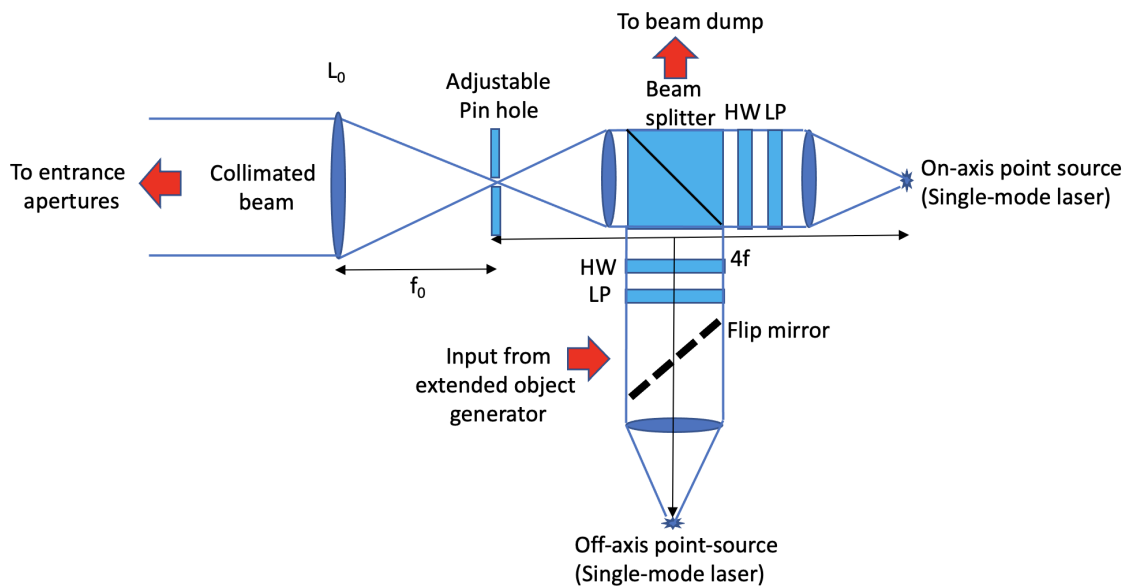
Figure 4.7 The set up for the, off-axis, object generator module: here, HW is a half-wave plate and LP is a linear polarizer. The off-axis point source is mounted on a precision x-y translation stage which allows the user to input varying separations between the two point sources. Each point-source (5 μm single mode fiber) laser has its own control allowing for a large range in contrast.

The extended-ObGen makes use of a double pass off an SLM where one pass inputs the phase information and the other the amplitude; using a similar approach to that of Jesacher et al. (2008). This combination allows for non-point source objects to be tested through any

system; objects we've begun testing for include simplistic shapes, the Hubble Telescope, and Jupiter. There is some difficulty though in using the SLMs with this method due to the discretization of the phase screens on the SLMs. As mentioned in the beginning of Section 1.4.1, the SLMs being used for our experiments are 8-bit meaning they only accept values between $0 - 255$. For phases the difference in values is usually enough that this is not a large issue, but for the amplitude pass (using the Bochner variables) this causes most of the information to go to zero. A way around this, potentially, is to input the amplitude information as a phase, thus shrinking the range of values needed; being that the phase is defined between 0 and 2π, the discretization will have a lesser impact than amplitude (which can vary over a much greater range). We have implemented a simple, phase only, solution on a single pass; though this is plagued with a ZODS. An amplitude pass would still be desired, as shown in Jesacher et al. (2008), but we have not yet been successful.

The simplistic ObGen, off-axis source, is currently installed onto the ARES system while the extended-ObGen has gone through an initial test and is in the process of being updated. Our "first-light" image of the Hubble telescope has successfully been made (Figure 4.8); and now begins the process of improving the image. We also tested making an image of a spotted star, Figure 4.9, which is of special interest in this work as it could lead to testing AGB or light-curve targets through our ARES instrument.

4.3 Discussion of Instrumentation Results

In this chapter we have detailed the status, plans, and results of our instruments being built in the optics lab at GSU.

We have an atmospheric turbulence generator in the ARES instrument. Using two SLMs we can simulate two layers of atmosphere (more if performing a double pass off the same SLM) and change the simulated distance between these layers with a motorized optical trombone between them. Further distance propagation can be obtained by changing the simulated telescope or adding in further path offsets from the 4-F system. We have shown:

one method of removing the ZODS, the ability of ARES to simulate a wide range of PSFs, and ARES's capability in correcting the wavefront with AO compensation (Figures 4.2, 4.3, 4.5 respectively), and the other applications for ARES (Section 4.1.3).

As well, we have detailed one other instrument, an object generator. The simplistic version, the off-axis source (Figure 4.7), is installed and currently being tested upon ARES. The extended object generator, capable of producing non-point source objects to send through our systems (Figure 4.8), is nearly done with it's preliminary tests and performs a double pass of a single SLM.
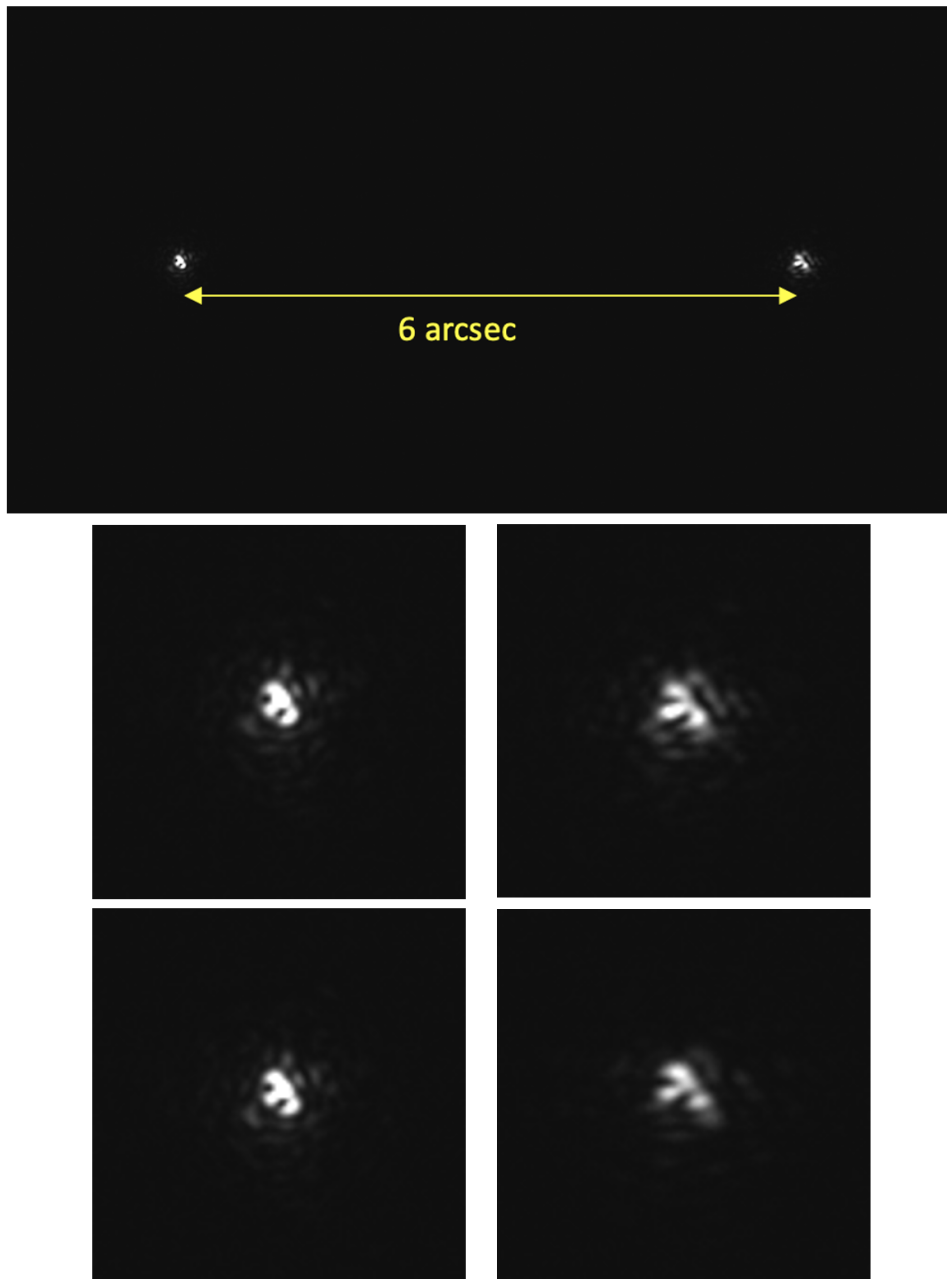
Figure 4.6 Here we show our preliminary results for the testing of anisoplantic imaging. The top image shows the two beams, made using the off-axis object generator shown in Section 4.2.1, separated by a simulated 6 arcseconds. For the next two rows, the left column shows the on-axis source with the off-axis source shown in the cut-out on the right. In the middle row, the beams are imaged in the pupil of the instrument, while in the bottom row there is a simulated propagation distance of 19km. Of note here is how the on-axis beam sees little to no change when the propagation is introduced whilst the off-axis source changes to a much more noticeable degree.
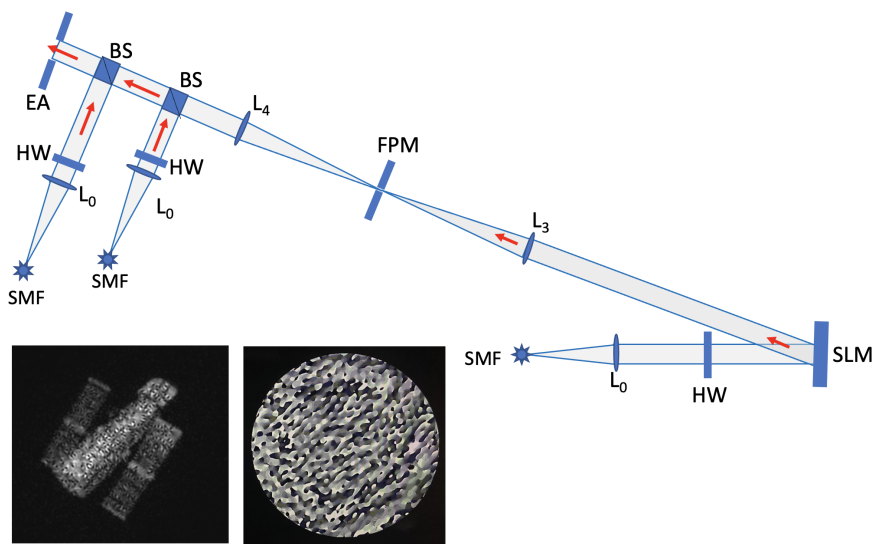
Figure 4.8 Here is a preliminary image of the Hubble telescope made by our extended object generator, schematic shown here as well. This is made by doing a phase only pass off a single SLM which inputs the phase information needed such that the an image of the desired object or pattern is formed.
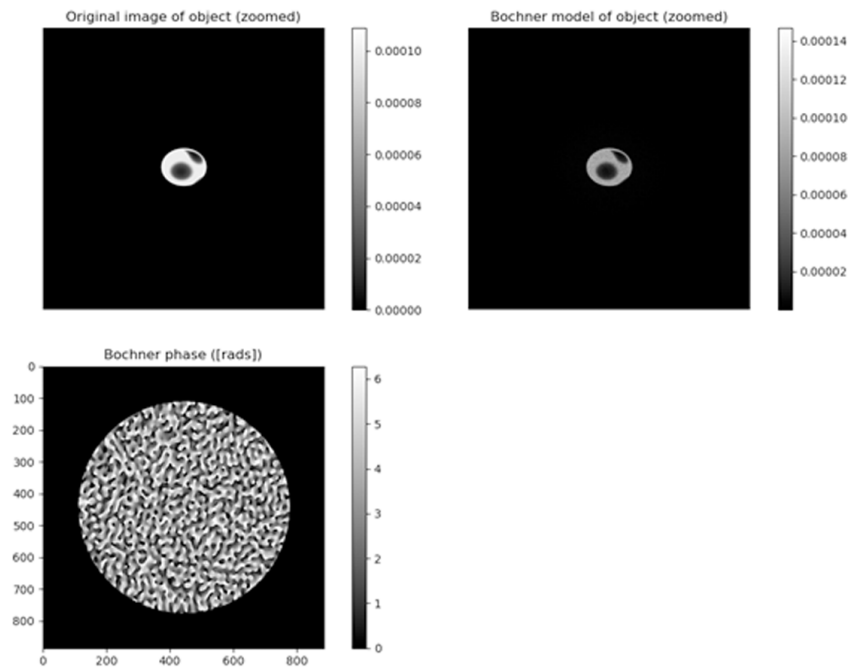
Figure 4.9 Here is an example image of a spotted star, specifically the Bochner phase to be input on the SLM, to be input on the ObGen. The top row shows the original image (left) and what the Bochner model will reproduce (right), with the second row image showing the Bochner phase that reconstructs that image. Such an object could be used to test image reconstructions of AGB stars or LI targets, both of which are of great interest in this work.

Chapter 5
CONCLUSION AND FUTURE DIRECTION

5.1 Where to find the code?

The codes made by our group shown here, OITOOLS and ROTIR, along with others can be found on GitHub (`https://github.com/fabienbaron`) and are coded in Julia. Specifically, ROTIR is found at `https://github.com/fabienbaron/ROTIR.jl` and OITOOLS at `https://github.com/fabienbaron/OITOOLS.jl`. All code is open-source and continuously being updated as new versions and new sciences are added.

5.2 Future Work

What follows is a summary of directions the research can be expanded upon and continued. While some are lofty and beyond the reach of a singular graduate student (namely the instrumentation projects) the others remain in realistic places with attainable goals.

5.2.1 *AGB Imaging*

Our goal for this project is to carry a mini-survey of AGBs which will broaden the scope of the project to the evolution of convection cells. The resulting images will be confronted with the most up-to-date radiative transfer models, similar to those done in (Paladini et al. 2018a). For this task we selected a representative sample of AGB stars with different chemistry and variability that we will observe with MIRC-X. For C-type targets, we will attempt to image the (possibly) dust-obscured discs to improve our understanding of the dust emission process. For the M-type and S-type targets, we will attempt to go beyond imaging the convection cells as done on π Gruis, and also try to assess their timescale of evolution by analyzing the multiple snapshots separated by time. A future plan, that also ties this project into the others, would be compare our interferometric reconstructions with ones made by LI by observing the flux of the star over time; combining the two methods should be able to give a sum greater than its parts.

We also have the continued collaborative projects with π Gru and RZ Ari. Pi Gru especially is a project of great interest given the many spectral channels of GRAVITY and the possible information therein. The new GRAVITY data, plus ever evolving image reconstruction techniques, makes interferometric imaging of AGBs an increasingly fascinating field to follow.

5.2.2 LI with ADMM

In the future we wish to expand upon ADMM and use it to pursue new machine learning techniques such as Expected Patch Likelihood (EPLL). With EPLL, or similar processes, performing LI will be even further enhanced and open further restoration pathways.

Furthermore, we wish to expand the code for more geometries, such as binaries, and more in depth simulations. As a part of this, improving the simulator to be able to do more complex spot geometries and non-linear changes to size, shape, temperature, and etc is of topmost priority.

5.2.3 Instrumentation

There is always more tests and improvements that can be done in instrumentation. For our instruments, what remains to be explored is no exception.

For ARES, we have yet to test (but are very close to) the communication between the Downlink and Uplink legs such that the Uplink is pre-conditioned to correct the expected wavefront. We are very close to our first tests of this and remain hopeful that the results shall come out as expected. After this, beyond any future instruments upcoming researchers may explore, is to update and install the polychromatic simulator and object generator(s) to be able to test more complicated objects through our atmospheric turbulence simulator.

The object generator has had its first successful initial testing, creating an image (though noisy) of the Hubble Telescope. What remains is to refine the system, reduce the noise to clean up the beam, and place it on a mobile or optional placement such that it can be quickly

put in or taken out (depending on what sort of sources the user/instrument is wanting to test). Very soon, this will be able to be used to generate the image of a spotted star (with the surface changing over time); with this, we can then start to test the LI-ADMM algorithm mentioned throughout this work with real photons and not just computer simulations.

Within our optics lab we have the parts and means to continue building and testing these instruments. Furthermore, there is a knowledge base, procedures, and parts available to pursue other yet to be designed instruments.

5.3   Conclusion

We have shown here three research paths that, although distinct in many ways, all are connected through the imaging of spotted stars and how we can and hope to improve how we gather the science and what is done with it:

First, we examined AGB stars with interferometry; specifically taking a sample of different spectral types, over time, with the CHARA array. This project, of the three described, has the farthest to go until its original goals are met. Even so, we have showed here observations of twelve stars with analysis of their angular size in the sky for seven of these targets. Of special note here was the large (for CHARA targets) star RZ Ari, whose angular size agreed with previous estimates of its size and luminosity (Villaume et al. 2017); allowing our group to calculate the mass of the AGB (Konstantinova-Antova et al. 2021). As well, in this chapter, we disccued the collaborative effort with examining data from the star π Gruis, and the ongoing trials there with displaying and utilizing the sheer extent of the data available from GRAVITY observations.

Next, LI was detailed; a method that needs only flux and time (with assumed or determined stellar properties) to be able to reconstruct possible temperature maps of the stellar surface. We then combined this with ADMM, a minimization method useful not only for its adaptability with many regularizers, but also being a boost to efficiency with simple parallelization. Following this project in the future, we anticipate ADMM being the stepping

70

stone towards machine learning techniques and other advanced methods/algorithms. To test the code we developed a highly customizable simulator that can generate stellar surfaces with a wide range of spot parameters; and then, the simulator can allow these spots to vary with time, now making the light-curves much more interesting and non-static. The code was then further tested on *Kepler* and *TESS* light-curve data, with the *Kepler* data being compared to other reconstruction methods (Roettenbacher et al. 2013; Thiebaut 2014) that used the same data.

Lastly, we covered the instruments and tests performed in the optics lab. We showed ARES, our highly adaptable testbed for atmospheric turbulence simulations (both down and back up through the atmosphere) and the progress with simulating atmospheric turbulence with phase screens. Next, we discussed our object generators and the status of the two versions (the "simplistic" and extended ObGen); included here was a very fresh image of an image of the Hubble telescope made with only two phase screens with a double pass off a SLM. In this chapter we also covered some of the future plans and other applications of both of these instruments (and others coming down the pipe). We emphasize here again that everything on the tables can be used together, with the future plan (combining ARES, the ObGen, and polychromatic simulator) being to have the capability of simulating any object source, at multiple wavelengths, going through nearly any amount of atmospheric turbulence; with optional AO. This means that in the near future we could test the LI-ADMM code with not just computer made simulations, but with actual photons on a real setup.

This work has showed the imaging of non-uniform stars in three unique, but interconnected, ways. AGBs are the observations, instruments take the observations, and LI uses the observations in additional ways. We look forward to the bright future, to where new designs and new methods of analysis shall take science.

References

Abbott, C. G., Baron, F., & Martinez, A. O. in prep A

Abbott, C. G., Johns, D., Jefferies, J. M., et al. 2022, in Technical Papers, Advanced Maui Optical and Space Surveillance Technologies (AMOS) Conference Series

ALPAO. 2021, Deformable Mirrors Datasheet, ALPAO. `https://www.alpao.com/products-and-services/deformable-mirrors/`

Anugu, N., Le Bouquin, J.-B., Monnier, J. D., et al. 2018, in Society of Photo-Optical Instrumentation Engineers (SPIE) Conference Series, Vol. 10701, Optical and Infrared Interferometry and Imaging VI, ed. M. J. Creech-Eakman, P. G. Tuthill, & A. Mérand, 1070124, doi: `10.1117/12.2313036`

Anugu, N., Le Bouquin, J.-B., Monnier, J. D., et al. 2020, AJ, 160, 158, doi: `10.3847/1538-3881/aba957`

Baron, F., & Martinez, A. O. 2018, ROTIR: Interferometric imaging and light curve inversion on rotating spheroids. `https://github.com/fabienbaron/ROTIR.jl`

Baron, F., Monnier, J. D., & Kloppenborg, B. 2010, in Society of Photo-Optical Instrumentation Engineers (SPIE) Conference Series, Vol. 7734, Optical and Infrared Interferometry II, ed. W. C. Danchi, F. Delplancke, & J. K. Rajagopal, 77342I, doi: `10.1117/12.857364`

Baron, F., Norris, R. P., & Martinez, A. O. 2019, OITOOLS: the All-in-One Tool Package for Optical Interferometry. `https://github.com/fabienbaron/OITOOLS.jl`

Borucki, W. J., Koch, D., Basri, G., et al. 2010, Science, 327, 977, doi: `10.1126/science.1185402`

Chan, S. H., Khoshabeh, R., Gibson, K. B., Gill, P. E., & Nguyen, T. Q. 2011, IEEE Transactions on Image Processing, 20, 3097. `http://videoprocessing.ucsd.edu/~stanleychan/deconvtv`

Claret, A., & Bloemen, S. 2011, A&A, 529, A75, doi: `10.1051/0004-6361/201116451`

Cowan, N. B., Fuentes, P. A., & Haggard, H. M. 2013, Monthly Notices of the Royal Astronomical Society, 434, 2465, doi: `10.1093/mnras/stt1191`

Cruzalèbes, P., Jorissen, A., Rabbia, Y., et al. 2013, MNRAS, 434, 437, doi: `10.1093/mnras/stt1037`

Dayton, D., Spencer, M., Hassall, A., & Rhoadarmer, T. 2018, in Society of Photo-Optical Instrumentation Engineers (SPIE) Conference Series, Vol. 10772, Unconventional and Indirect Imaging, Image Reconstruction, and Wavefront Sensing 2018, 107720H, doi: `10.1117/12.2319968`

De Beck, E., & Olofsson, H. 2018, A&A, 615, A8, doi: `10.1051/0004-6361/201732470`

Deledalle, C.-A., Parameswaran, S., & Nguyen, T. Q. 2018. `https://hal.archives-ouvertes.fr/hal-01700082`

Eriksson, K., Nowotny, W., Höfner, S., Aringer, B., & Wachter, A. 2014, A&A, 566, A95, doi: 10.1051/0004-6361/201323241

Figueiredo, M. A. T., & Bioucas-Dias, J. M. 2010, IEEE Transactions on Image Processing, 19, 3133, doi: 10.1109/TIP.2010.2053941

Fleischer, A. J., Gauger, A., & Sedlmayr, E. 1992, A&A, 266, 321

Freytag, B., & Höfner, S. 2008, A&A, 483, 571, doi: 10.1051/0004-6361:20078096

Gaia Collaboration, Prusti, T., de Bruijne, J. H. J., et al. 2016, A&A, 595, A1, doi: 10.1051/0004-6361/201629272

Gehan, C., Mosser, B., Michel, E., & Cunha, M. S. 2021, A&A, 645, A124, doi: 10.1051/0004-6361/202039285

Gizon, L., & Solanki, S. K. 2003, ApJ, 589, 1009, doi: 10.1086/374715

GRAVITY Collaboration, Abuter, R., Accardo, M., et al. 2017, A&A, 602, A94, doi: 10.1051/0004-6361/201730838

Habing, H. J., & Olofsson, H. 2004, in Asymptotic Giant Bracnh Stars

Harmon, R. O., & Crews, L. J. 2000, AJ, 120, 3274, doi: 10.1086/316882

Hoefner, S., & Dorfi, E. A. 1997, A&A, 319, 648

Jesacher, A., Maurer, C., Schwaighofer, A., Bernet, S., & Ritsch-Marte, M. 2008, Opt. Express, 16, 2597, doi: 10.1364/OE.16.002597

Jorissen, A., Frayer, D. T., Johnson, H. R., Mayor, M., & Smith, V. V. 1993, A&A, 271, 463

Käpylä, P. J., Mantere, M. J., & Hackman, T. 2011, ApJ, 742, 34, doi: 10.1088/0004-637X/742/1/34

Konstantinova-Antova, R., Georgiev, S., Lèbre, A., et al. 2021, in The 20.5th Cambridge Workshop on Cool Stars, Stellar Systems, and the Sun (CS20.5), Cambridge Workshop on Cool Stars, Stellar Systems, and the Sun, 194, doi: 10.5281/zenodo.4566012

Kraus, S., Monnier, J. D., Anugu, N., et al. 2018, in Society of Photo-Optical Instrumentation Engineers (SPIE) Conference Series, Vol. 10701, Optical and Infrared Interferometry and Imaging VI, ed. M. J. Creech-Eakman, P. G. Tuthill, & A. Mérand, 1070123, doi: 10.1117/12.2311706

Lane, R. G., Glindemann, A., & Dainty, J. C. 1992, Waves in Random Media, 2, 209, doi: 10.1088/0959-7174/2/3/003

Lattanzio, J. C., & Wood, P. R. 2004, Evolution, Nucleosynthesis, and Pulsation of AGB Stars, ed. H. J. Habing & H. Olofsson (New York, NY: Springer New York), 23–104, doi: 10.1007/978-1-4757-3876-6_2

Lazarev, G., Chen, P.-J., Strauss, J., Fontaine, N., & Forbes, A. 2019, Opt. Express, 27, 16206, doi: 10.1364/OE.27.016206

Le Bouquin, J.-B. 2020, MIRC-X data reduction pipeline. https://gitlab.chara.gsu.edu/lebouquj/mircx_pipeline

Liou, M.-S. 1995, Journal of Computational Physics, 118, 294, doi: https://doi.org/10.1006/jcph.1995.1100

Liu, G., Huang, T.-Z., Lv, X.-G., & Liu, J. 2013, arXiv e-prints, arXiv:1312.6813. https://arxiv.org/abs/1312.6813

Luger, R., Agol, E., Foreman-Mackey, D., et al. 2019, The Astronomical Journal, 157, 64, doi: 10.3847/1538-3881/aae8e5

Maehara, H., Notsu, Y., Namekata, K., et al. 2021, PASJ, 73, 44, doi: 10.1093/pasj/psaa098

Majeau, C., Agol, E., & Cowan, N. B. 2012, The Astrophysical Journal, 747, L20, doi: 10.1088/2041-8205/747/2/l20

Martinez, A. O. 2021, PhD thesis, Georgia State University

Martinez, A. O., Baron, F. R., Monnier, J. D., Roettenbacher, R. M., & Parks, J. R. 2021, ApJ, 916, 60, doi: 10.3847/1538-4357/ac06a5

McAlister, H. A., ten Brummelaar, T. A., Gies, D. R., et al. 2005, ApJ, 628, 439, doi: 10.1086/430730

Meadowlark. 2019, User Manual 1920x1152 XY Phase Series Spatial Light Modulator with HDMI Controller, Meadowlark Optics, Inc. www.meadowlark.com

Monnier, J. D., Berger, J.-P., Le Bouquin, J.-B., et al. 2014, in Proc. SPIE, Vol. 9146, Optical and Infrared Interferometry IV, 91461Q, doi: 10.1117/12.2057312

Monnier, J. D., Le Bouquin, J.-B., Anugu, N., et al. 2018, in Society of Photo-Optical Instrumentation Engineers (SPIE) Conference Series, Vol. 10701, Optical and Infrared Interferometry and Imaging VI, ed. M. J. Creech-Eakman, P. G. Tuthill, & A. Mérand, 1070122, doi: 10.1117/12.2312762

Nelson, J., Mast, T., & Chanan, G. 2013, Segmented Mirror Telescopes, ed. T. D. Oswalt & I. S. McLean (Dordrecht: Springer Netherlands), 99–136, doi: 10.1007/978-94-007-5621-2_3

Paladini, C. 2011, PhD thesis

Paladini, C., Aringer, B., Hron, J., et al. 2009, A&A, 501, 1073, doi: 10.1051/0004-6361/200911938

Paladini, C., Baron, F., Jorissen, A., et al. 2018a, Nature, 553, 310, doi: `10.1038/nature25001`

—. 2018b, The Messenger, 172, 24, doi: `10.18727/0722-6691/5077`

Roettenbacher, R. M., Harmon, R. O., Vutisalchavakul, N., & Henry, G. W. 2011, AJ, 141, 138, doi: `10.1088/0004-6256/141/4/138`

Roettenbacher, R. M., Monnier, J. D., Harmon, R. O., Barclay, T., & Still, M. 2013, ApJ, 767, 60, doi: `10.1088/0004-637X/767/1/60`

Schutz, A., Ferrari, A., Mary, D., et al. 2014, Journal of the Optical Society of America. A Optics, Image Science, and Vision, 31, 2334, doi: `10.1364/JOSAA.31.002334`

Sedmak, G. 2004, Appl. Opt., 43, 4527, doi: `10.1364/AO.43.004527`

Simões, M., Almeida, L. B., Bioucas-Dias, J., & Chanussot, J. 2016, IEEE Transactions on Image Processing, 25, 5266, doi: `10.1109/TIP.2016.2603920`

ten Brummelaar, T. A., McAlister, H. A., Ridgway, S. T., et al. 2005, ApJ, 628, 453, doi: `10.1086/430729`

Thiebaut, E. 2002, in Astronomical Data Analysis II, ed. J.-L. Starck & F. D. Murtagh, Vol. 4847, International Society for Optics and Photonics (SPIE), 174 – 183, doi: `10.1117/12.461151`

Thiebaut, E. 2014, OptimPak. `https://github.com/emmt/OptimPack`

van Belle, G. T., Paladini, C., Aringer, B., Hron, J., & Ciardi, D. 2013, ApJ, 775, 45, doi: `10.1088/0004-637X/775/1/45`

Van Den Oord, A., & Schrauwen, B. 2014, J. Mach. Learn. Res., 15, 2061–2086

van Eck, S., Neyskens, P., Plez, B., et al. 2011, in Astronomical Society of the Pacific Conference Series, Vol. 445, Why Galaxies Care about AGB Stars II: Shining Examples and Common Inhabitants, ed. F. Kerschbaum, T. Lebzelter, & R. F. Wing, 71. `https://arxiv.org/abs/1011.2092`

van Leeuwen, F., de Bruijne, J., Babusiaux, C., et al. 2022, Gaia DR3 documentation, Gaia DR3 documentation, European Space Agency; Gaia Data Processing and Analysis Consortium. Online at ¡A href="https://gea.esac.esa.int/archive/documentation/GDR3/index.html"¿https://gea.esac.esa.int/arch id. 1

Villaume, A., Conroy, C., Johnson, B., et al. 2017, ApJS, 230, 23, doi: `10.3847/1538-4365/aa72ed`

Willson, L. A. 2000, ARA&A, 38, 573, doi: `10.1146/annurev.astro.38.1.573`

Wittkowski, M., Boboltz, D. A., Ireland, M., et al. 2011, A&A, 532, L7, doi: `10.1051/0004-6361/201117411`

Wittkowski, M., Hofmann, K.-H., Höfner, S., et al. 2017, A&A, 601, A3, doi: `10.1051/0004-6361/201630214`

Xu, Z., Figueiredo, M. A. T., Yuan, X., Studer, C., & Goldstein, T. 2017, in 2017 IEEE Conference on Computer Vision and Pattern Recognition (CVPR), 7234–7243, doi: `10.1109/CVPR.2017.765`

Zoran, D., & Weiss, Y. 2011, in 2011 International Conference on Computer Vision, 479–486, doi: `10.1109/ICCV.2011.6126278`

EXTRA IMAGES AND PLOTS
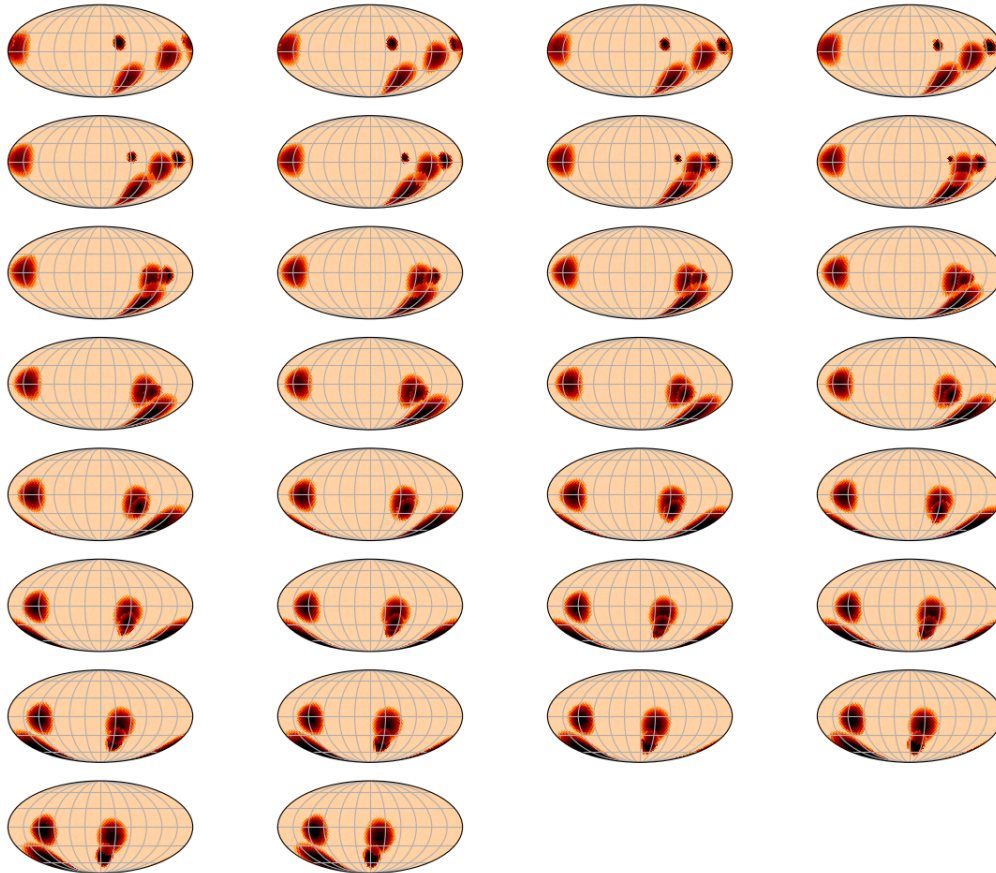
Figure A.1 This figure shows the true surfaces generated by Simulation 3 from Section 3.2.4.
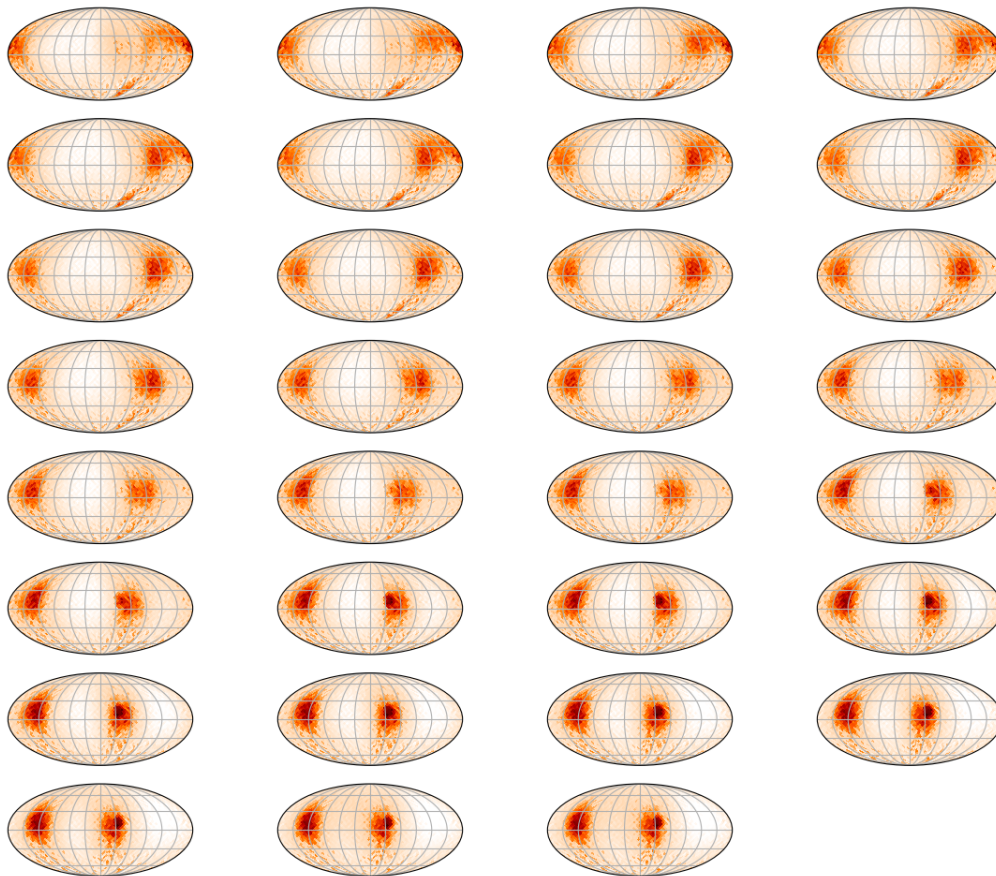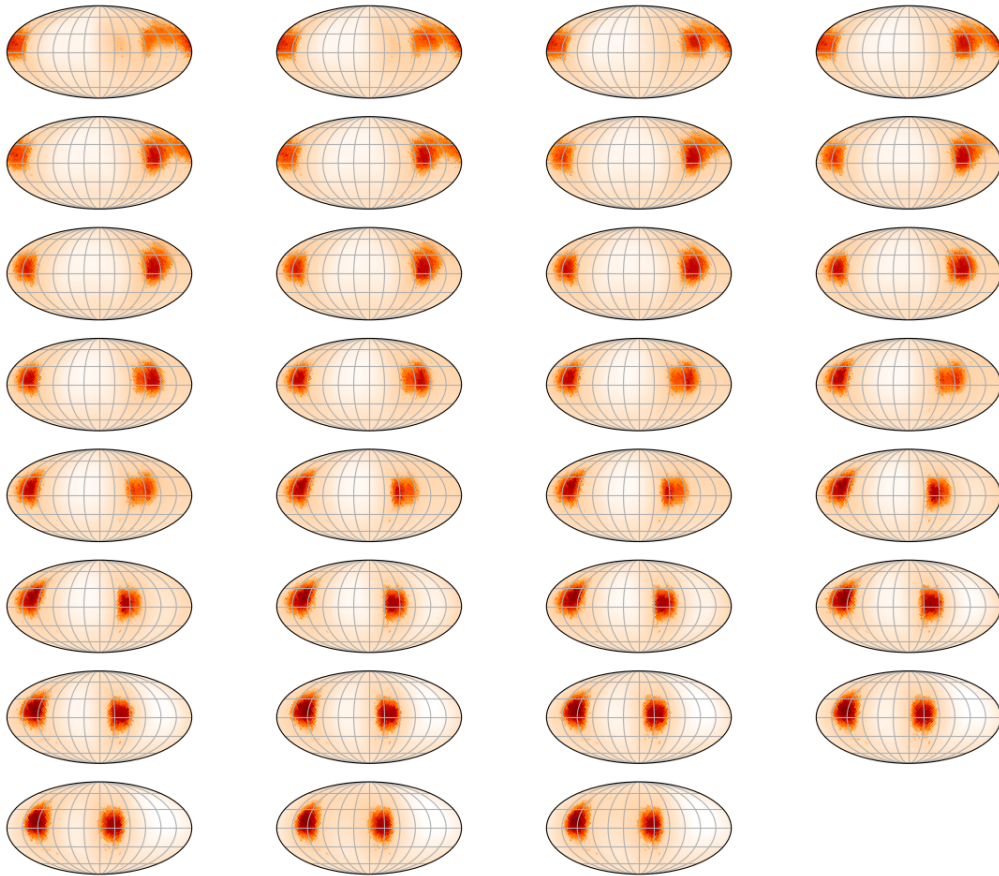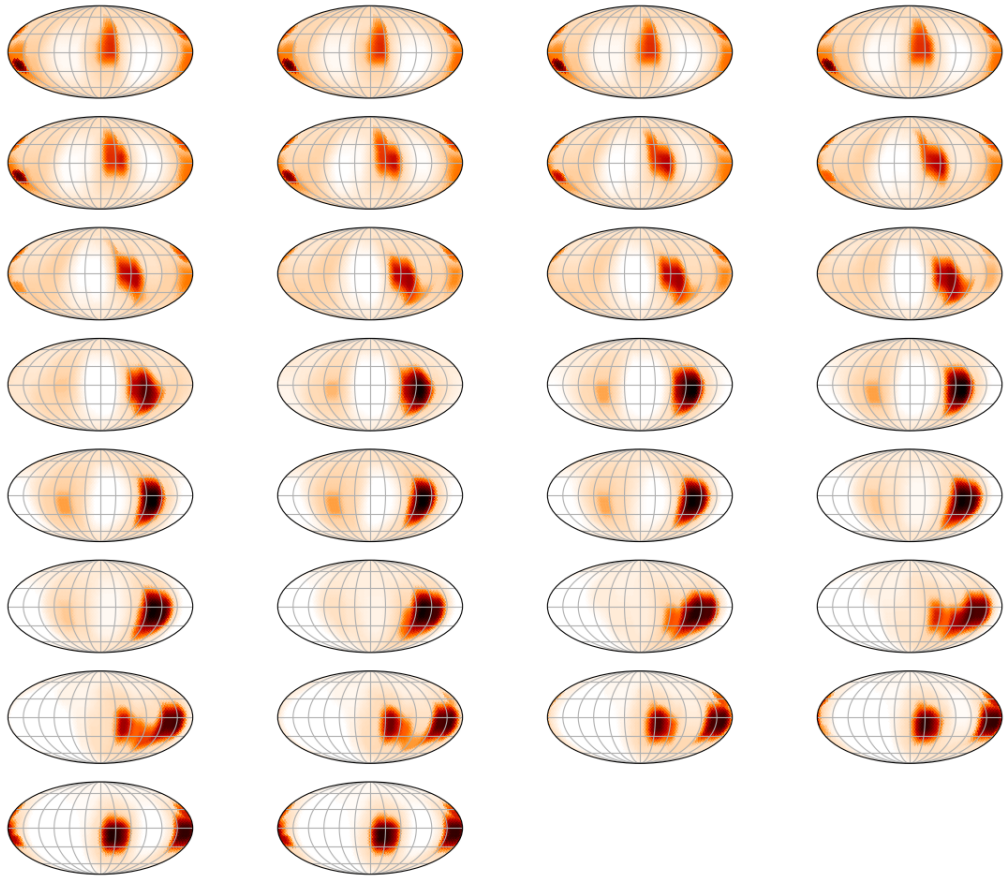
Figure A.2 This figure shows the full results of the reconstruction for Simulation 1 with our ADMM-LI code, starting with the truth images (with added noise) for the initial guesses. The truth images are shown in Figure A.1.
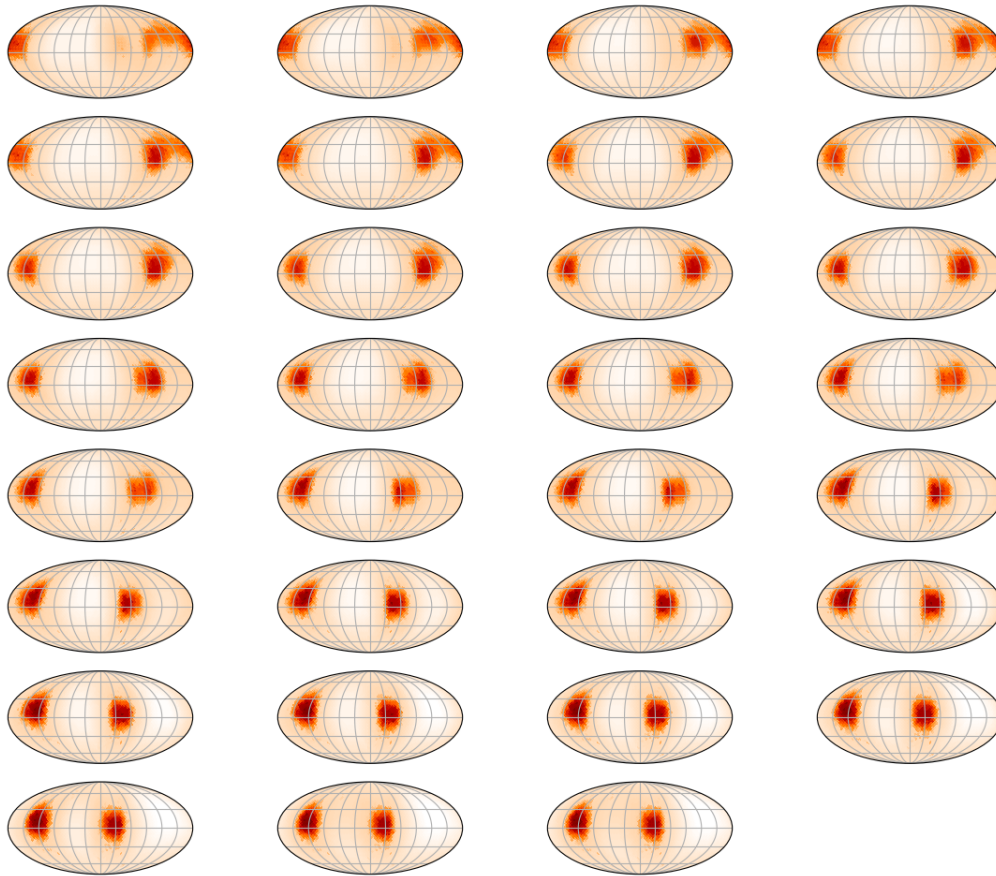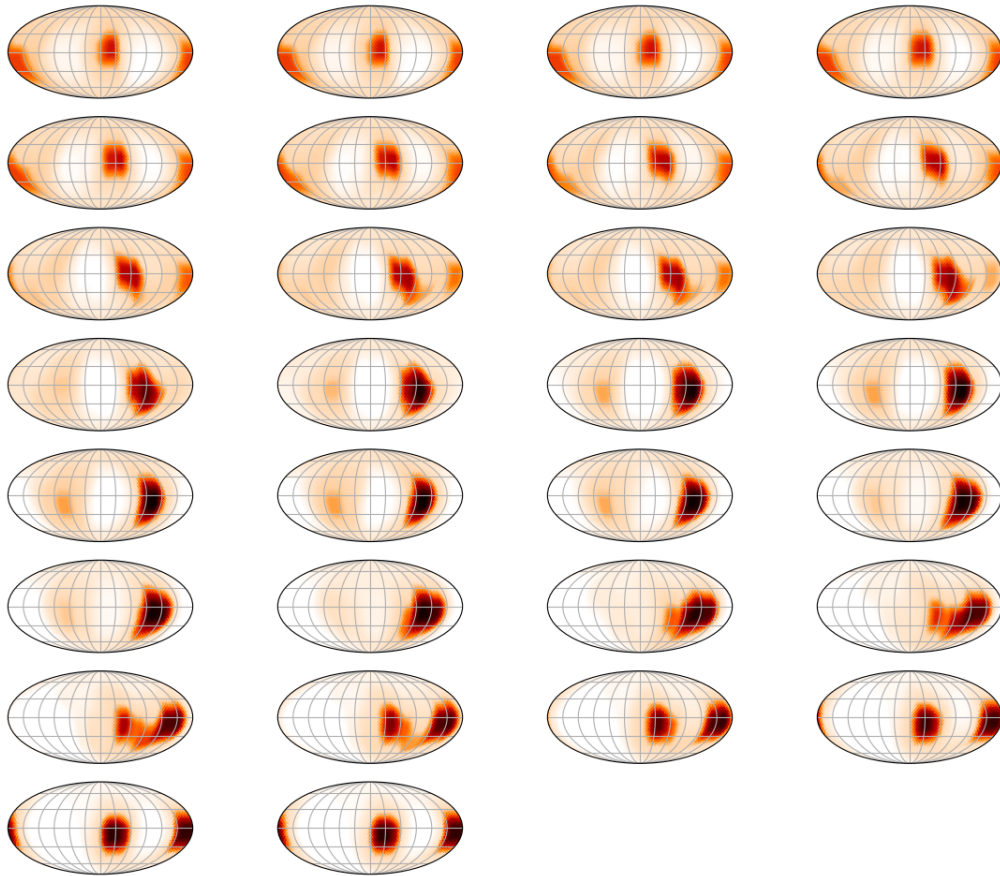
Figure A.3 This figure shows the full results of the reconstruction for Simulation 1 with our ADMM-LI code, starting with flat images of the average surface temperature for the initial guesses. The truth images are shown in Figure A.1.
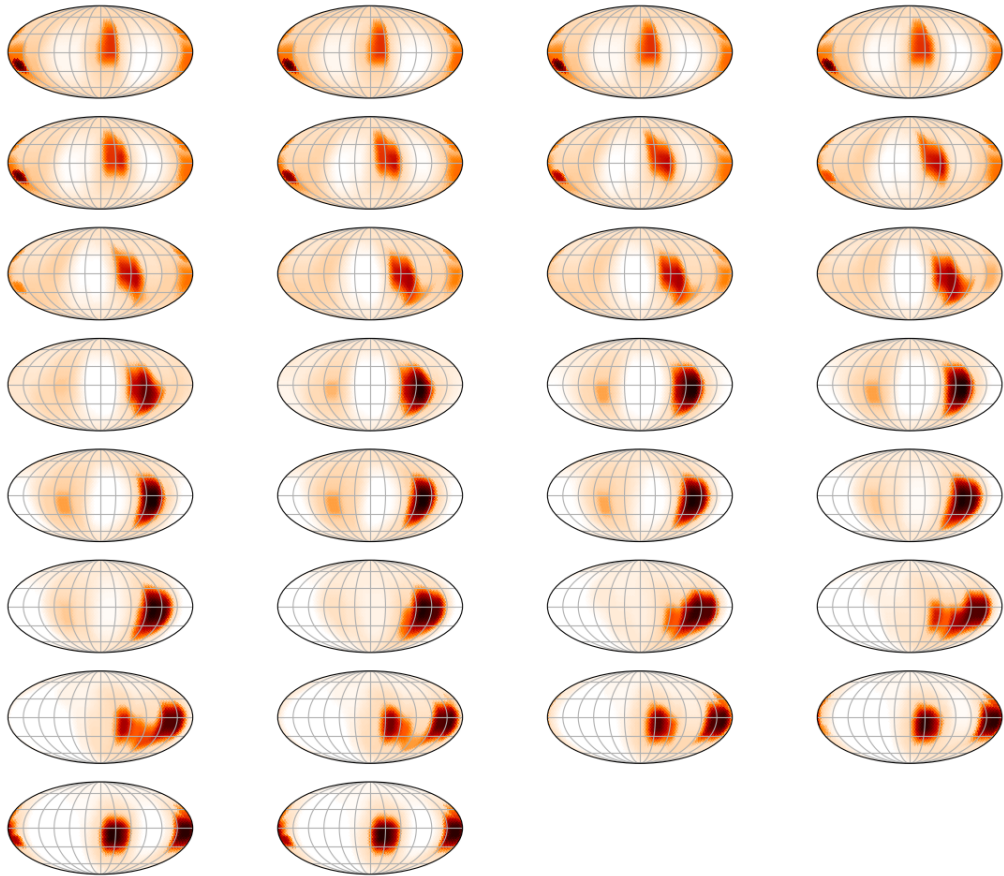
Figure A.4 This figure shows the full results of the reconstruction for Simulation 1 with our ADMM-LI code, starting with random maps for the initial guesses. The truth images are shown in Figure A.1.
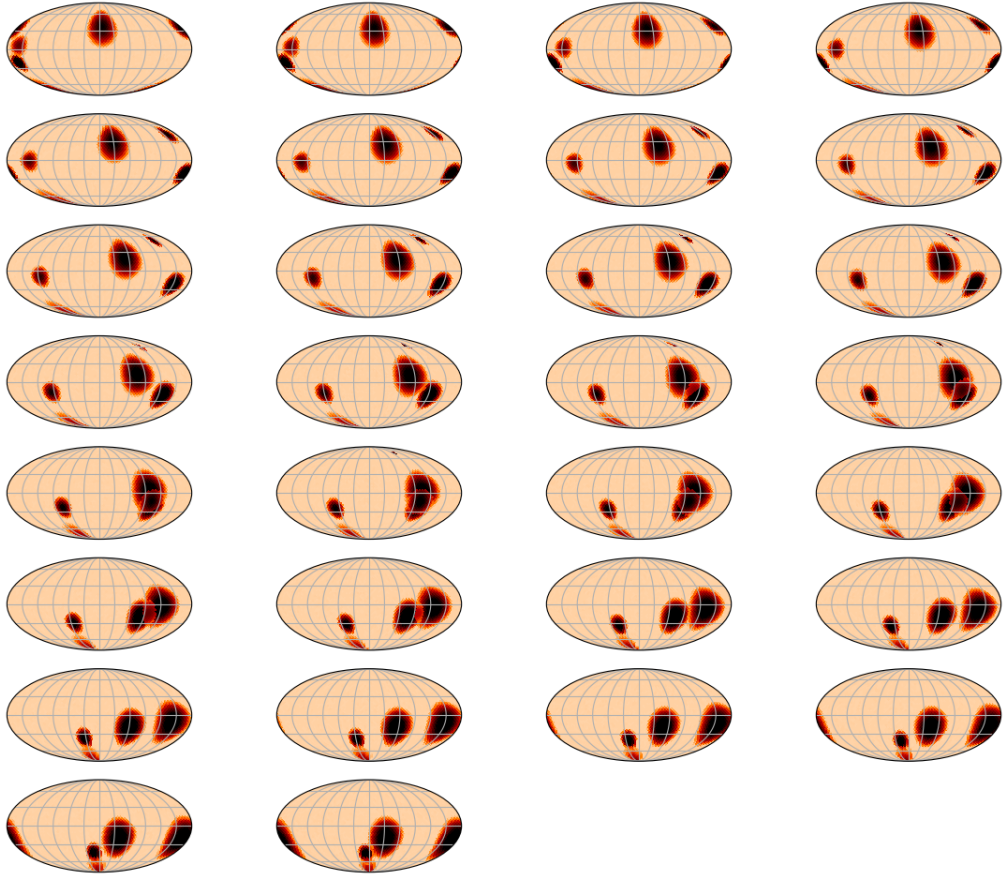
Figure A.5 This figure shows the full truth images of Simulation 4 from Section 3.2.4.

Figure A.6 This figure shows the full results of Simulation 4 with its reconstruction with our ADMM-LI code, starting with the truth images (with added noise) for the initial guesses. The truth images are shown in Figure A.5.

Figure A.7 This figure shows the full results of Simulation 4 with its reconstruction with our ADMM-LI code, starting with flat images of the average surface temperature for the initial guesses. The truth images are shown in Figure A.5.

Figure A.8 This figure shows the full results of Simulation 4 with its reconstruction with our ADMM-LI code, starting with random maps for the initial guesses. The truth images are shown in Figure A.5.
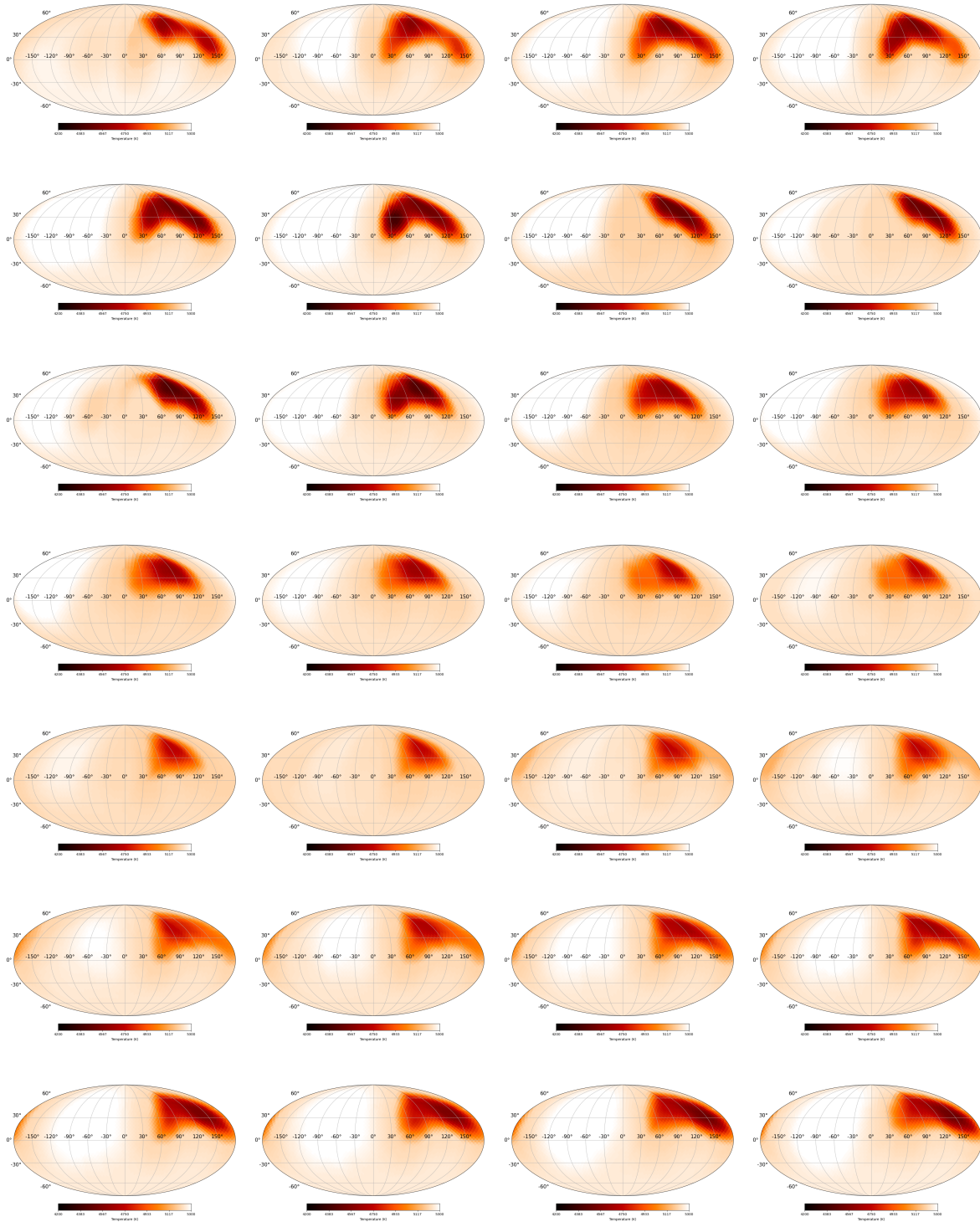
Figure A.9 This figure shows the full ADMM reconstruction for KIC 5110407 (detailed in Section 3.3). The remaining plots, of the 52 total epochs, are shown in Figure A.10.
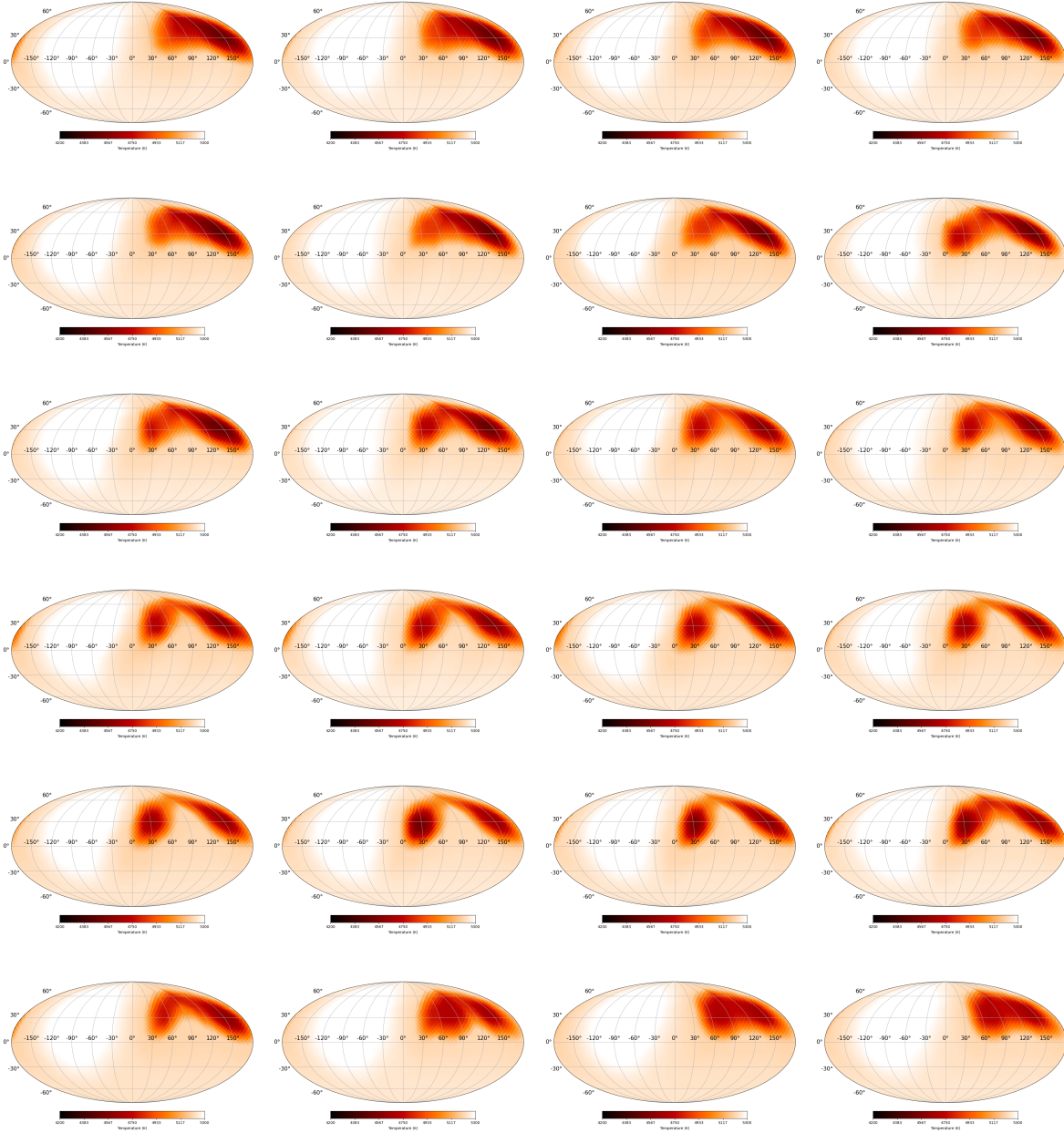
Figure A.10 This figure shows the full ADMM reconstruction for KIC 5110407 (detailed in Section 3.3 for the epochs not included in Figure A.9.
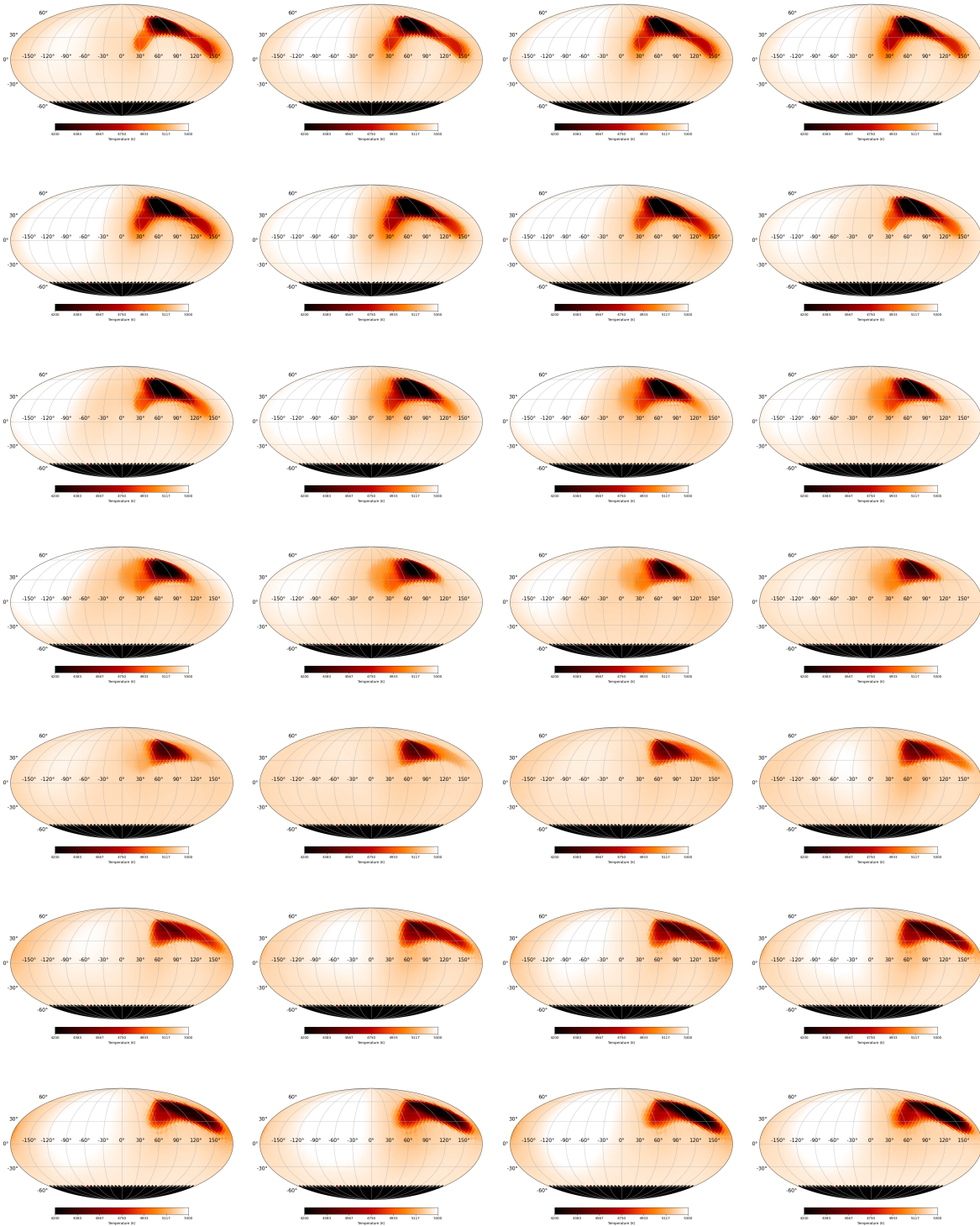
Figure A.11 This figure shows the full OptimPak reconstruction for KIC 5110407 (detailed in Section 3.3). The remaining plots, of the 52 total epochs, are shown in Figure A.12.
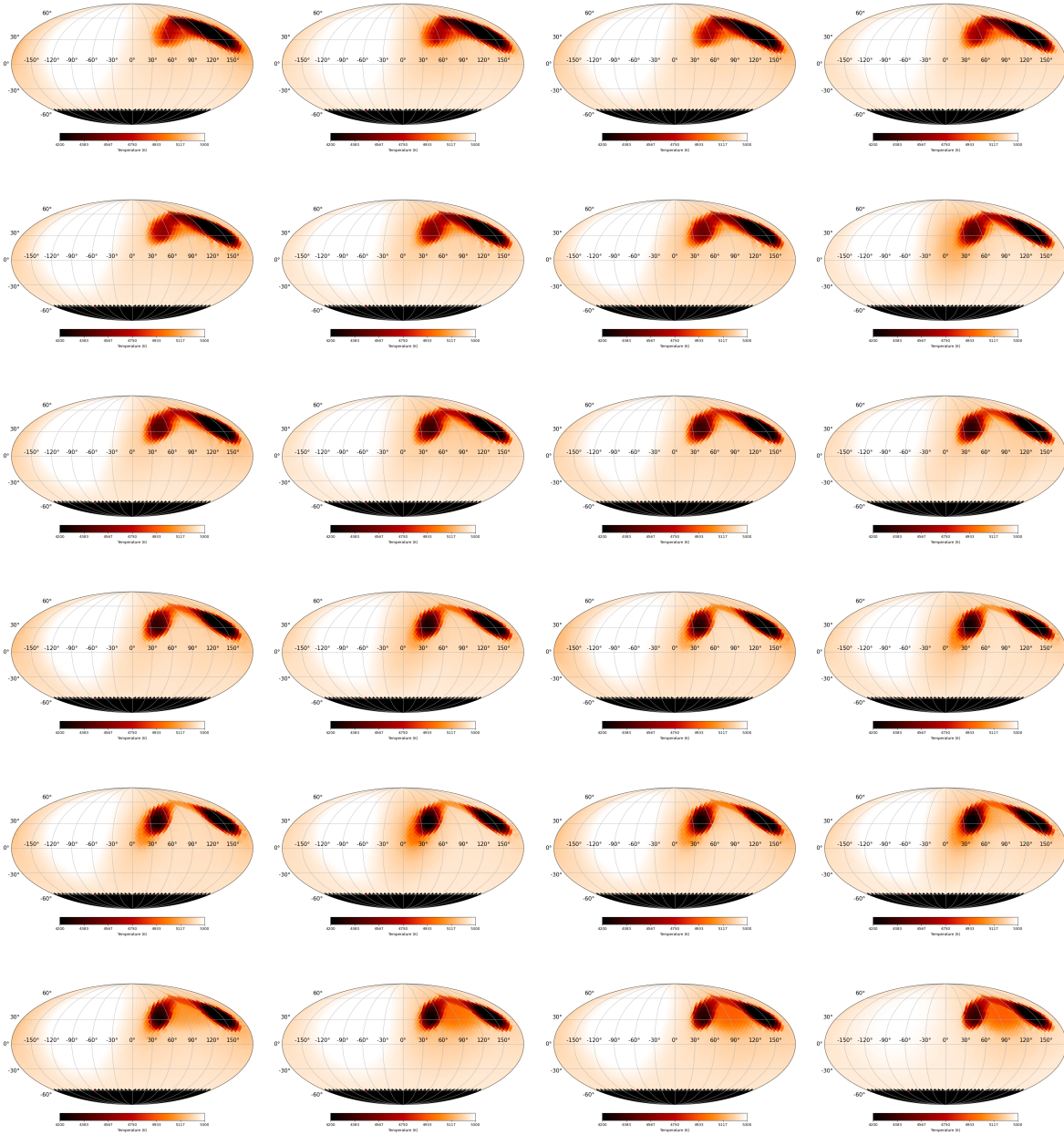
Figure A.12 This figure shows the full OptimPak reconstruction for KIC 5110407 (detailed in Section 3.3 for the epochs not included in Figure A.11.
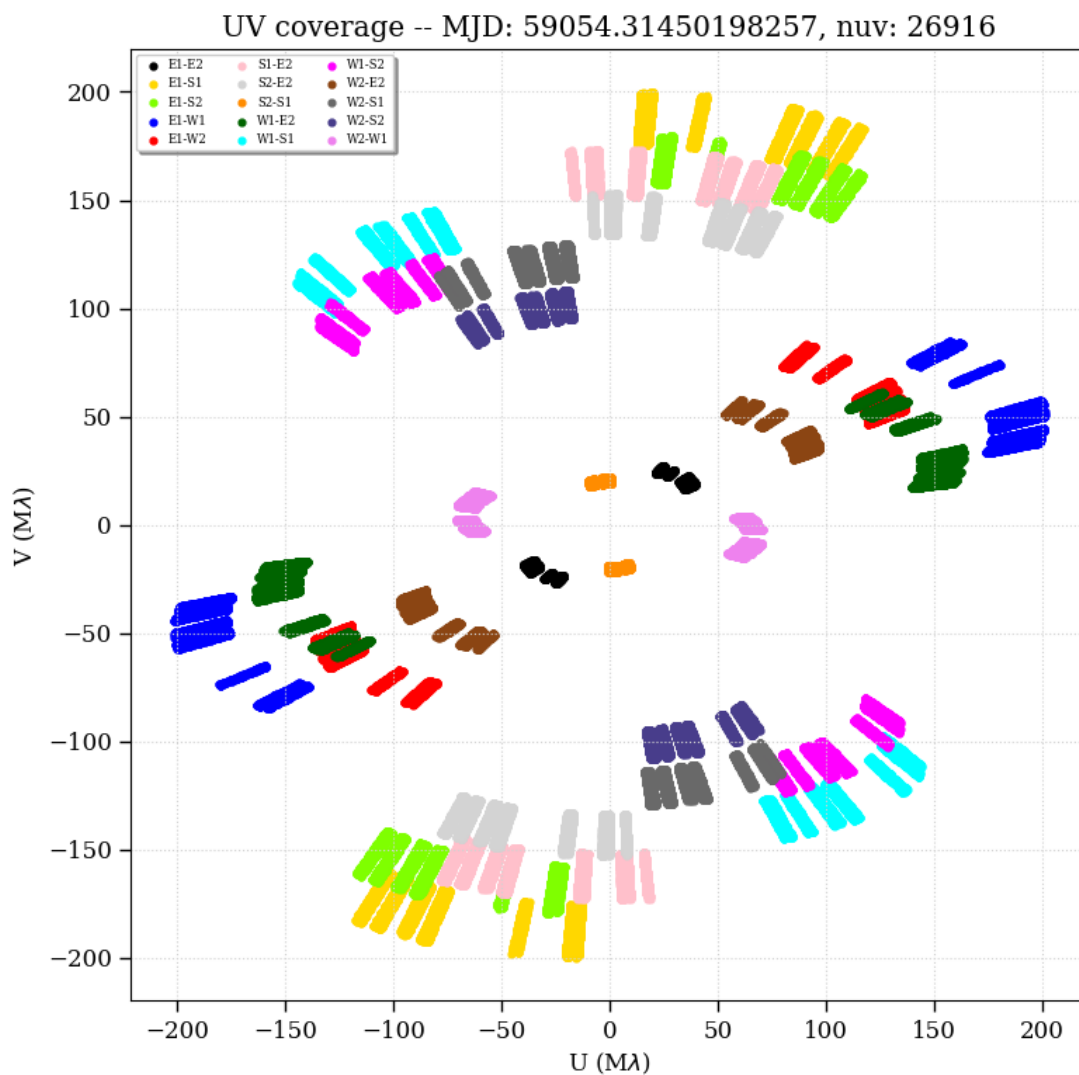
Figure A.13 An example of the UV data gathered (for HR Peg in this case) from CHARA using all six telescopes (Section 2.2). This data corresponds to multiple observations over the course of a month.